วิธีสังเคราะห์และควบคุมของการเคลื่อนที่ด้วยตนเองของละอองแกลเลียมบนแกลเลียมอาร์เซไนด์ (001) ในเครื่องปลูกผลึกด้วยลำโมเลกุล

นายเบนี อาดิ ทริสนา

วิทยานิพนธ์นี้เป็นส่วนหนึ่งของการศึกษาตามหลักสูตรปริญญาวิศวกรรมศาสตรมหาบัณฑิต
สาขาวิชาวิศวกรรมไฟฟ้า ภาควิชาวิศวกรรมไฟฟ้า
คณะวิศวกรรมศาสตร์ จุฬาลงกรณ์มหาวิทยาลัย
ปีการศึกษา 2557

RELIABLE SYNTHESIS AND MANIPULATION OF SELF-RUNNING GALLIUM DROPLETS ON GALLIUM ARSENIDE (001) IN MBE

Mr. Beni Adi Trisna

A Thesis Submitted in Partial Fulfillment of the Requirements
for the Degree of Master of Engineering Program in Electrical Engineering
Department of Electrical Engineering
Faculty of Engineering
Chulalongkorn University
Academic Year 2014

Thesis Title	RELIABLE SYNTHESIS AND MANIPULATION OF SELF-RUNNING GALLIUM DROPLETS ON GALLIUM ARSENIDE (001) IN MBE
By	Mr. Beni Adi Trisna
Field of Study	Electrical Engineering
Thesis Advisor	Associate Professor Songphol Kanjanachuchai, Ph.D.

Accepted by the Faculty of Engineering, Chulalongkorn University in Partial Fulfillment of the Requirements for the Master's Degree

.....Dean of the Faculty of Engineering
(Professor Bundhit Eua-arporn, Ph.D.)

THESIS COMMITTEE

.....Chairman
(Professor Somsak Panyakaew, Ph.D.)

.....Thesis Advisor
(Associate Professor Songphol Kanjanachuchai, Ph.D.)

.....External Examiner
(Anurat Wisitsoraat, Ph.D.)

เบนี อาดิ ทริสนา : วิธีสังเคราะห์และควบคุมของการเคลื่อนที่ด้วยตนเองของละอองแกลเลียมบนแกลเลียมอาร์เซไนด์ (001) ในเครื่องปลูกผลึกด้วยลำโมเลกุล (RELIABLE SYNTHESIS AND MANIPULATION OF SELF-RUNNING GALLIUM DROPLETS ON GALLIUM ARSENIDE (001) IN MBE) อ .ที่ปรึกษาวิทยานิพนธ์หลัก: รศ. ดร. ทรงพล กาญจนชูชัย, หน้า.

วิทยานิพนธ์ฉบับนี้รายงานวิธีสังเคราะห์และควบคุมละอองแกลเลียมที่เคลื่อนที่ด้วยตนเองบนแกลเลียมอาร์เซไนด์ (001) ในเครื่องปลูกผลึกด้วยลำโมเลกุล (Molecular Beam Epitaxy, MBE) ชิ้นงานถูกศึกษาโดยกล้องจุลทรรศน์แรงอะตอม (Atomic Force Microscopy) กล้องจุลทรรศน์แบบเปรียบต่างการแทรกสอดเชิงอนุพันธ์ (Differential Interference Contrast Microscopy) และกล้องจุลทรรศน์อิเล็กตรอนแบบส่องกราด (Scanning Electron Microscopy) ส่วนสมบัติเชิงไฟฟ้าศึกษาโดยการวัดความสัมพันธ์กระแส-แรงดัน (Current-Voltage)

ขั้นตอนที่นำเสนอทำให้สามารถใช้เทคนิค MBE สังเคราะห์ละอองแกลเลียมที่เคลื่อนที่ด้วยตนเองได้โดยให้ผลที่น่าเชื่อถือแม้จะขาดความสามารถในการมองเห็นภาพตามเวลาจริงก็ตาม ขั้นตอนที่ว่าอาศัยการสังเกตแบบรูปการเลี้ยวเบนอิเล็กตรอนพลังงานสูงที่ตกกระทบผิวหน้า และการเปรียบเทียบกับอุณหภูมิอ้างอิงที่เหมาะสม ตามด้วยการควบคุมโพรไฟล์การระเหิด ผิวหน้าระหว่างละอองแกลเลียมกับแกลเลียมอาร์เซไนด์ถูกตรวจสอบเชิงไฟฟ้า ผลเบื้องต้นจากการวัดกระแส-แรงดันชี้ว่ารอยต่อแสดงพฤติกรรมแบบช็อตต์กี

วิทยานิพนธ์ฉบับนี้ได้เสนอวิธีควบคุมละอองแกลเลียมที่เคลื่อนที่ด้วยตนเองโดยใช้จุดบกพร่องที่ฝังอยู่ด้านล่างและสาธิตให้เห็นด้วยกล้องจุลทรรศน์อิเล็กตรอนแบบพลังงานต่ำ (Low-Energy Electron Microscope) โดยได้ค้นพบว่าแกลเลียมนั้นวิ่งและเลี้ยวอย่างฉับพลันเมื่อเจอกับจุดบกพร่องที่อาจเกิดขึ้นจากการถ่มของแกลเลียม ผลดังกล่าวได้ให้ข้อมูลเชิงลึกแบบใหม่เกี่ยวกับการเคลื่อนที่ของละอองแกลเลียมและอาจจะทำให้มีโอกาสในการควบคุมทิศทางการเคลื่อนที่ของละอองแกลเลียมก็เป็นได้

ภาควิชา วิศวกรรมไฟฟ้า ลายมือชื่อนิสิต .....

สาขาวิชา วิศวกรรมไฟฟ้า ลายมือชื่อ อ.ที่ปรึกษาหลัก .....

ปีการศึกษา 2557

5670501521 : MAJOR ELECTRICAL ENGINEERING
KEYWORDS: SELF-RUNNING DROPLETS / RHEED / MOLECULAR BEAM EPITAXY / LOW-ENERGY ELECTRON MICROSCOPY / DROPLETS TURNING

BENI ADI TRISNA: RELIABLE SYNTHESIS AND MANIPULATION OF SELF-RUNNING GALLIUM DROPLETS ON GALLIUM ARSENIDE (001) IN MBE. ADVISOR: ASSOC. PROF. SONGPHOL KANJANACHUCHAI, Ph.D., pp.

A procedure for reliable synthesis and the attempts to manipulate self-running Ga droplets on GaAs (001) in a molecular beam epitaxial (MBE) machine have been investigated. The running Ga droplets are studied by atomic force microscopy, differential interference contrast microscopy, and scanning electron microscopy. Their electrical properties are characterized by current-voltage (*I-V*) measurements.

Using the proposed procedure, the formation of self-running Ga droplets has been reliably achieved in MBE despite the lack of real-space and real-time imaging capability. The procedure is based on the observation of in situ reflection high-energy electron diffraction patterns and the registration of an appropriate reference temperature followed by controlled sublimation profiles. The Ga droplet-GaAs interface is probed electrically; preliminary *I-V* measurements indicate that the interface shows a Schottky behavior.

The manipulation of self-running Ga droplets migration using buried defects is proposed and demonstrated in a low-energy electron microscope. The Ga droplets are found to run and take sharp turns upon meeting with defects, possibly from Ga-spitting. Such results provide new insights of the running droplets dynamics and may open up opportunities to steer the droplets motion.

Department: Electrical Engineering Student's Signature .....
Field of Study: Electrical Engineering Advisor's Signature .....
Academic Year: 2014

ACKNOWLEDGEMENTS

First praise is to God, Allah S.W.T, the almighty who protecting and guiding me to finish this thesis. This thesis has successfully completed because of the assistance and advice of several peoples. Hence, I would like to express my sincere thanks to all them.

My deepest appreciation goes to my supervisor, Associate Professor Songphol Kanjanachuchai, Ph.D., whose constructive comments and encouragements were very valuable. I would like to thank the committee members: Professor Somsak Panyakeow, Ph.D., and Anurat Wisitsoraat, Ph.D., for their importance advices during the thesis preparation. I am also deeply thankful to our colleagues at Semiconductor Device Research Laboratory and the beamline 3.2b of the Thai's Synchrotron Light Research Institute. I am thanks to Mr. Nitas Nakareseisoon and Mr. Win Eiwwongcharoen for their assistance in MBE.

I am so grateful to the Chulalongkorn University Asean scholarship program for making it possible for me to study here. I also appreciate the financial support from Thailand's National Research University Project, Office of the Higher Education Commission (WCU-036-EN-57) for funding my research.

I am also thanks to all my friends in Indonesia and Thailand: Mr. Yosi Aristiawan, Mrs. Anis Kristiani, Mrs. Eka Triwahyuni, Mr. Pamuko Aditya Rahman, Mr. Doni Marisi Sinaga, and Mr. Nguyên Thi Cao for the joyful gatherings and emotional supports.

I am thanks to my parent: Mr. Suyanto and Mrs. Sri Suharti and my parent in-law: Mr. Ridwan Heryanto and Mrs. Herni Rahmawati. Your prayer and sacrifice were what support me thus far. I owe a lot to my lovely wife and daughter: Mrs. Dilla Meyfana Erniawan and Ms. Refeyfa Eloise Trisna for being my source of constant and unconditional love.

Finally, I would like to thank everyone else I forget to mention who supported and helped me during my study.

CONTENTS

Page

Page

Page

LIST OF FIGURES

LIST OF SYMBOLS

$\gamma_{vs(l)}$	surface free energy associated to liquidus chemical potential
a_1 and a_2	coefficients from the reference viscosity table
μ^0	1 mPa s
α	coefficient of dynamic and kinetic properties of surface
θ	contact angle between γ_{ls} and γ_{vl}
δ	contact angle between γ_{vs} and γ_{vl}
φ	contact angle between γ_{vs} and γ_{ls}
U	contact line velocity or dR/dt
c	damping coefficient
d	diameter of droplet
F_{diff}	diffusion force along diffusion barrier orientation
F_{drift}	drift force resulted from spatial variation of $\Delta\mu$
R	droplet base radius
h_d	droplet height
μ	droplet's viscosity
υ_f	friction term of running droplet
F_m	maximum force
m	mobility or the inverse damping coefficient ($1/c$)
F_{tot}	net force vector of running droplet
$\gamma_{vs(s)}$	surface free energy associated to surface chemical potential
μ_s	surface Ga chemical potential
μ_l	surface Ga liquidus chemical potential
γ_{ls}	surface tension of liquid-solid interface

γ_{vl}	surface tension of vapor-liquid interface
γ_{vs}	surface tension of vapor-solid interface
υ	velocity of droplet
F_v	viscos force
Δx	surface step
2D	two dimensional
3D	three dimensional
A	junction area
A^*	Richardson's constant
AFM	atomic force microscopy
Al	aluminum
As	arsenide
As_2 or As_4	arsenide
As_2O_3	arsenic trioxide
b	burger vector
CCD	charge-coupled device
CHPs	cross-hatch patterns
Cu	copper
C-V	capacitance-voltage
DIC	differential interference contrast
E_c	conduction band
ECCI	electron channeling contrast imaging
EDS	energy dispersive spectra
E_f	fermi level
E_{fi}	intrinsic Fermi level
E_v	valence band
$\mathbf{e}_x$	x unit vector
$\mathbf{e}_y$	y unit vector
F_μ	running force of droplet when approaching a dislocation
FM	Frank-van de Merwe
F_σ	local force due to a buried dislocation

G	shear modulus
Ga	gallium
Ga_2O	gallium(I) oxide
Ga_2O_3	gallium(III) oxide
GaAs	gallium arsenide
h	depth of buried dislocation
H_2O	water
H_2O_2	hydrogen peroxide
H_3PO_4	phosporic acid
HCl	hydrochloric acid
I	current
IBSCs	intermediate band solar cells
I_{dark}	dark current
In	indium
InAs	indium arsenide
InGaAs	indium gallium arsenide
InP	indium phosphide
InSb	indium antimonide
I_{sat}	reverse saturation current
J_{sc}	short circuit current
I-V	current-voltage
k_BT	thermal energy
KOH	potassium hydroxide
LED	light emitting diode
LEEM	low-energy electron microscopy
MBE	molecular beam epitaxy
MDs	misfit dislocations
MS	metal-semiconductor
n	ideality factor
nm	nanometer
NW	nanowire

OIM	optical interference microscopy
OM	optical microscope
P	phosphide
PEEM	photoemission electron microscopy
PID	proportional-integral-derivative
P_{max}	maximum power
QD	quantum dot
RGA	residual gas analyzer
RHEED	reflection high-energy diffraction
RMS	root mean square
SCM	scanning confocal microscopy
SEM	scanning electron microscopy
SEM	scanning electron microscopy
SiO_x	silicon oxides
SK	Stranski-Krastanov
SSM	scanning stylus microscopy
STM	scanning tunneling microscopy
T	sample temperature
T_0	reference temperature
T_A	active temperature
T_c	congruent evaporation temperature
UHV	ultra-high vacuum
UV	ultraviolet
v	poisson's ratio
V	voltage
V_b	applied bias voltage
V_{bi}	built-in voltage
VLS	vapor-liquid-solid
V_{oc}	open circuit voltage
VW	Volmer-Weber
W	tungsten

WL	wetting layer
σ	surface stress
σ_{yy}	surface stress component perpendicular to a dislocation line
σ_{yzz}	surface stress component parallel to a dislocation line
Φ_B	Schottky barrier height
Φ_{B0}	ideal barrier height

CHAPTER 1
Introduction

The study in this thesis covers extensive research on the fabrication and characterization of nanostructures especially on self-running droplets. A lot of works related to self-running droplets have been conducted using molecular beam epitaxy (MBE) machine. The fundamental understanding of running droplet mechanism and characteristics are explained which could significantly improve the understanding of droplet growth based design.

The first chapter presents several general topics, which will be explained in details in further chapters.

1.1 Nanotechnology and Nanostructures

Nanotechnology is one of the research disciplines which study the material in nanometer (nm) size. Nanotechnology have been developing in various independent research fields, e.g., physics, biology, and medical science. In term of physics of solid state study, the nano-sized materials are commonly called nanostructures. In addition, the material can be called nanostructures when at least one length scale in it is less than or equal to 100 nm. For example, if we have a box, then one side of the box has to be less than or equal to 100 nm, while the others side can be infinite. There are many kind of nanostructures which already known e.g., quantum wells, quantum wires, and quantum dots, many of which formed from metallic droplets.

Figure 1.1 shows various length scales and physical shape of matters, including nanostructures. The smallest unit of matter that defines the chemical element is an atom. Furthermore, 100 times larger than atom, there is quantum dot (QD) structures which were discovered at the first time in 1981 by Ekimov et al [1]. QD stuctures are still under research for their ultimate applications, for example, in high conversion efficiency intermediate band solar cells (IBSCs) [2]. Further structure, having length ten times longer than QD, there is nanowire (NW) structrure. The fabrication process of nanowire uses droplets as growth catalyst in the so-called vapor-liquid-solid (VLS) growth [3]. The diamater of nanowire is equal to droplet catalyst diameter, around 100 nm, making them one kind of nanostructures. The last

structure on which this thesis will focuss, is running Ga droplets. In 2009, Tersoff et al. [4] reported a new droplet dynamics on semiconductor surface. They observed running Ga droplets from Langmuir evaporation of GaAs (001). The diameter and height of running Ga droplet are about 1.9 μm [5] and 1.4 μm [6], respectively, making running Ga droplet cannot be categorized as nanostructures. However in other running metallic droplet/semiconductor substrates, Au/Si, running Au droplets have found with diameter as small as 20 nm [7] and putting them into the category of nanostructures. So running droplet studies are classified as nano- and microtechnology.

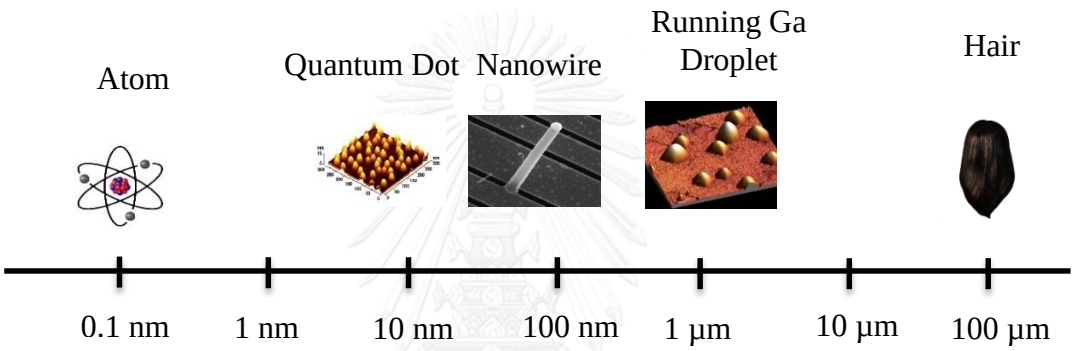

Figure 1.1 Overview of the length scales of physical nanostructures.

1.2 Droplet and Self-Running Properties

Droplets can be used for a lot of functions. In solar cell technology, droplets have been used as efficient anti-reflection coating [8]; they also improve the solar cell energy conversion via surface plasmons [9]. In droplet epitaxy, droplets are principal starting material, e.g., in the fabrication of intersublevel infrared photodetector with strain-free GaAs QDs [10] and single photon emitter [11]. Versatile functions of droplet has led to a resurgence of droplet dynamics studies including running droplets.

There are several studies on the running Ga droplets. Hilner et al. [12] investigated the self-running Ga droplets on GaP (111)B. They reported that the running mechanism is associated with nanoscale rouger step stimulation. This mechanism is different from Ga droplets on GaAs (001), which is associated with chemical potentils [4]. In addition, Kanjanachuchai et al. [13] investigated langmuir evaporation of GaAs (111) A and B surfaces. For GaAs (111)B, the running characteristic is similar to GaAs (001). This similarity may suggest that they have the

same driving force i.e., derive from chemical potentials. In contrast, in GaAs (111)A, the running directions for sliding and sticking droplets are directed by subsurface dislocation and crystallographic etching, respectively. The running mechanism of droplets that still controversial on various systems can be more understood if more running droplet studies are conducted.

The previous described studies are mainly conducted by in situ observation under a low-energy electron microscope (LEEM). The limited number of LEEM machine, causing some group to experiment using commonly available molecular beam epitaxy (MBE) [5, 6]. However, the realization of running droplets on MBE requires optimization and tricks because MBE is mainly used for deposition, not microscopy.

1.3 Objectives

The objectives of this study are to develop a reliable procedure for the synthesis of self-running Ga droplets in MBE, to do droplet *I-V* characterization, and to manipulate the migration of self-running Ga droplet in LEEM.

1.4 Outline

This thesis is organized as follows: droplets formation, self-running droplet mechanism and control are reviewed in chapter 2. The fundamental parameters to achieve self-running droplets are also presented. Chapter 3 shows experimental details of running droplets fabrication and characterization. The key results—reliable synthesis of self-running Ga droplets in MBE, droplet *I-V* characterization, and manipulation of the migration of self-running Ga droplets in LEEM—are presented in chapter 4. Finally, the summary and outlook are given in chapter 5.

CHAPTER 2
Backgrounds

Self-running droplets formation based on the Langmuir evaporation of substrate are reviewed in this chapter. Fundamental parameters to achieve self-running droplets are presented which explain why the running droplets phenomenon in semiconductor surface was more lately introduced than the other systems. The droplet force imbalance due to surface chemical potentials are reviewed to describe the running droplet mechanism. Droplet dynamics are explained in term of running trails, secondary droplets, wettability, and control. Finally, the manipulation of running droplet migration using cross-hatch patterns (CHPs) and the theory of metal-semiconductor (MS) junction are presented.

2.1 Forming Ga Droplets on GaAs Surface

Forming Ga droplets on GaAs surface is relatively a simple process. Droplets can be formed from evaporation of free surface or so-called Langmuir evaporation. Langmuir evaporation of GaAs above 585 °C, will readily induce the decomposition; the GaAs substances are broken down into As vapor and liquid metallic Ga. Decomposition happens due to a large different of vapor pressure between group III (Ga) and group V (As) that generates the sublimation of group V material and condensation of group III material into the droplets. Through decomposition, the clustering of Ga droplets can be formed on GaAs surface [14]. The important parameters of those droplets are density and size.

The density and size of droplets have been able to be adjusted by photolithography and wet chemical etching technique as explained by Li et al [15]. They characterize the sample by wet etching before Langmuir evaporation. The sample is covered by photoresist and etched by H_3PO_4: H_2O_2: H_2O (3:1:100). After chemical etching, the trench areas become etched areas while the strip top areas become un-etched areas. Then the sample is sublimated in Riber-32P solid-source MBE machine. After quenching the sample to room temperature, scanning electron microscopy (SEM) analysis is conducted. Figure 2.1 shows the disparity between the trench and strip top of the post-annealed sample. In the trench areas, the density of Ga

droplets is one order of magnitude higher than those on the strip top areas. However, the average size of the Ga droplets on the strip top areas is much larger than those on the trench areas. This experiment shows the ability of droplet density and size control using pre-patterned surface.

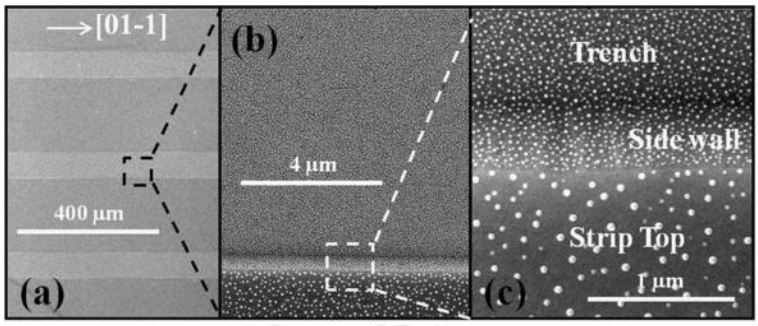

Figure 2.1 SEM images of the formation of Ga droplets on GaAs surface at the interface between the trench and strip areas [15].

Droplet density and size control may as well be done by real-time controlling the sample temperature [16]. Figure 2.2 shows the real-time observation of GaAs in photoemission electron microscopy (PEEM) during sublimation. In this experiment, in the beginning, the sample temperature is raised to above the critical temperature, the so-called congruent evaporation temperature T_c. Above T_c, due to a large difference of vapor pressure between Ga and As, As evaporates more rapidly than Ga, leading to condensation of Ga into droplets. The higher the temperature above T_c, the larger the size of Ga droplets since more Ga material incorporates to the droplets. The density of droplets also increases because Ga favor to accumulate on the surface. Subsequently, the sample temperature was then reduced below T_c as shown in Figure 2.2(a). The temperature cooling below T_c induces Ga droplets to shrink and disappear. The Ga droplet, marked with 1, is the largest observed and the latest disappeared droplet. Then, the sample temperature is gradually raised to 620 °C, causing the droplet marked with 1 reappear in the same position. This condition is stable with no other appearing droplet for temperature between 620 and 625 °C as shown in Figures 2.2(c) and 2.2(d). Upon the temperature rising to 635 °C, the second droplet, marked with 2, reappears in accordance to the previous position before the droplet disappears as shown on Figure 2.2(e). After several minutes, the others droplets appear with only

one new droplet appears at new position which marked by a triangle sign as shown in Figure 2.2(f). Hence, in this experiment, Tersoff et al. [16] have demonstrated some success in controlling the nucleation positions of Ga droplets on GaAs (001).

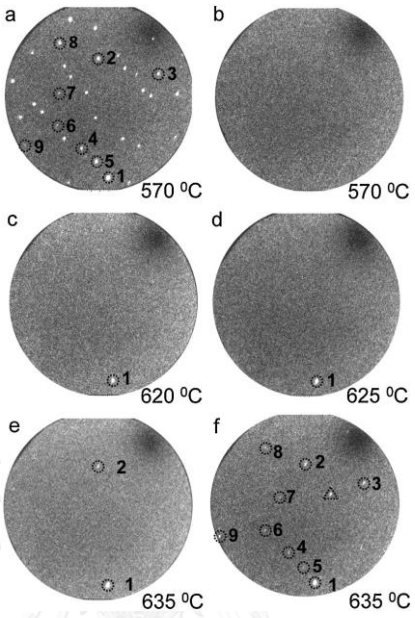

Figure 2.2 PEEM images of Ga droplets on GaAs (001) during the sublimation process [16].

2.2 Fundamental Requirement Parameters for Running Droplets

Running droplets were observed in various systems for about a century [17-19], but the first observation of running droplets on semiconductor surface was only lately discovered in 2009, using LEEM. The running mechanism requires stringent control of parameters which limits the observation in readily available system, i.e., MBE. Two important parameters in running droplets realization are pressure and temperature.

2.2.1 Pressure

To achieve self-running droplets during Langmuir evaporation, the system pressure has to be kept under ultra-high vacuum (UHV) condition. UHV condition is the condition when the system pressure is below 10^{-7} Pa or 10^{-9} Torr. Otherwise, if the pressure is between 10^{-4} and 10^{-5} Torr, the scanning electron microscopy (SEM)

vacuum chamber pressure, Langmuir evaporation will cause droplet etching, resulting in micro-scale holes on the sample surface [20].

Figure 2.3 demonstrated the formation process of micro-scale holes on GaAs (001) when the sample is sublimated in the SEM vacuum chamber. The residual oxygen in the chamber act as an etching catalyst by reacting with the Ga and resulting in the formation of Ga oxide or Ga_2O as shown from chemical reaction:

$$Ga_2O_3 + 4\ GaAs \rightarrow 3\ Ga_2O\uparrow + 2\ As_2\uparrow \qquad (2.1)$$

The size of holes is much bigger and deeper than the holes created by Ga-triggered nanodrill process [21]. The presence of oxide is obviously supporting the chemical drilling process to be more effective.

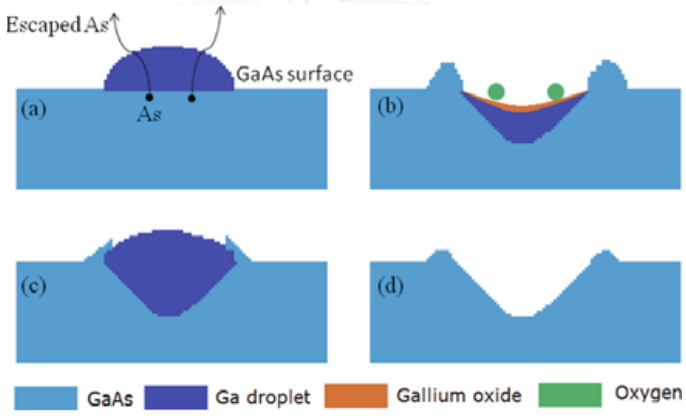

Figure 2.3 Schematic diagram of the occurrence of micro-scale holes on GaAs (001) surface due to the thermal etching process [20].

2.2.2 Temperature

The second fundamental parameter is temperature. Sample temperature must be increased above T_c to stimulate running droplets. However, the temperature must not be too low or high otherwise under- and over-decomposition, respectively, will result. Droplets are not formed in under decomposition, while the high density droplets due to late stage coalescence are formed in over-decomposition [14]. Both conditions yield no running droplets. Hence to produce running droplets, sample temperature must be optimized because it directly affects the droplet running force from surface chemical potential. The relation between temperature and surface checimal potential are explained in Section 2.3.

2.3 Surface Chemical Potential Towards Running Droplets

The chronology of self-running Ga droplets on GaAs (001) is shown in Figure 2.4. The GaAs surface condition is related to the surface Ga chemical potential (μ_s) and the surface Ga liquidus chemical potential (μ_l). In Langmuir evaporation below T_c, μ_s establishes condition where Ga and As evaporate at the same rates so that the GaAs surface remains flat. Above T_c, μ_s is higher than μ_l; As evaporates more rapidly than Ga, resulting in Ga droplets (3D structures) formation.

The schematic cross section of a Ga droplet is shown in Figures 2.4(a) and 2.4(b). The surface free energy associated with surface chemical potential and liquidus chemical potential are $\gamma_{vs(s)}$ and $\gamma_{vs(l)}$, respectively. The relation between these potentials and the net droplet driving force is given by [4]

$$F_{tot} = (\gamma_{vs(s)} - \gamma_{vs(l)})d = \alpha(T - T_c)^2 d \tag{2.2}$$

where F_{tot} is the net force vector, d is the diameter of the droplet, T is the sample temperature, and α is the coefficient of dynamic and kinetic properties of the surface. In immobile droplet, the net force is equal to zero; the net force has equal value around the perimeter as shown in Figure 2.4(a). While in mobile droplets, Figures 2.4(b) and 2.4(c), $\gamma_{vs(s)}$ is larger than $\gamma_{vs(l)}$; the net force is greater than zero, causing the droplet displacement [4].

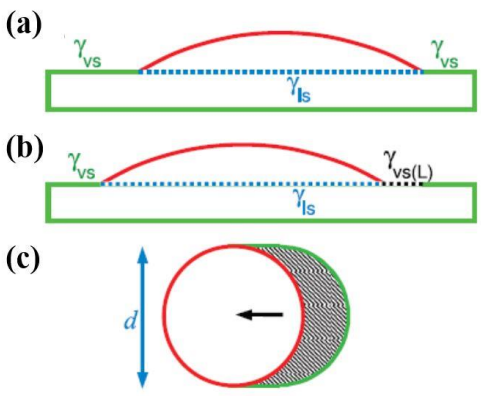

Figure 2.4 Schematic diagram of the self-running Ga droplets on GaAs (001) [4].

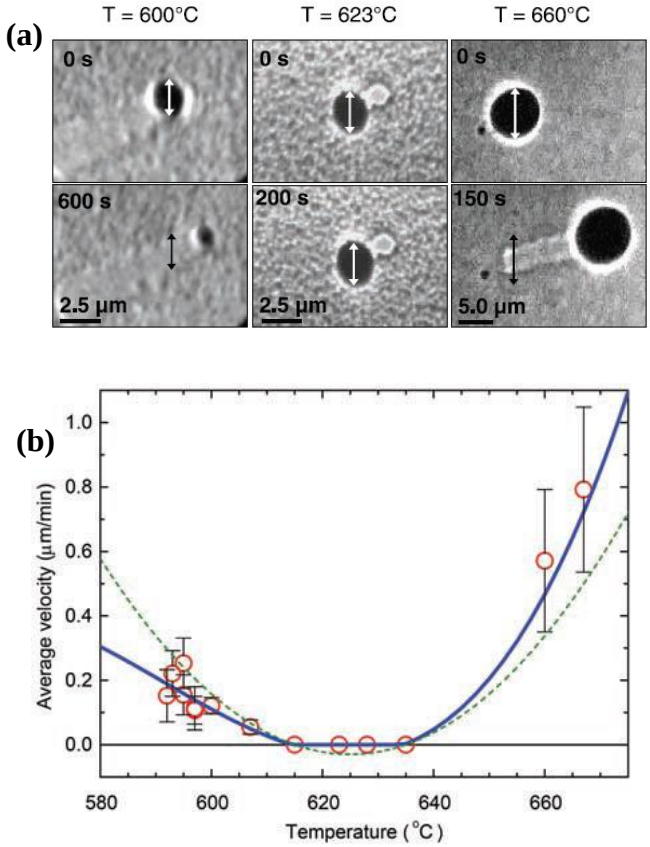

Figure 2.5 (a) Time-lapse images of running Ga droplets at various temperatures: below (left), within (center), and above (right) T_c (b) Temperature vs average droplet velocity of the self-running Ga droplets on GaAs (001) [4].

The following mathematical model is taken from the Supplementary Information to Tersoff's original paper [4] showed the correlation between $(T-T_c)^2$ and the droplet velocity υ. The linear damping mathematical model is

$$F = c\upsilon \tag{2.3}$$

The force vector and damping coefficient are represented as F and c, respectively. With an assumption that the stick-slip motion of Ga droplets as the time-average motion and a damped response to F_{tot}. F_{tot} consist s of the Ga droplets force due to surface chemical potential (*F*) and an effective friction opposite to the droplets motion

direction (F_f). Thus, the velocities include the Ga droplet velocity (υ) and the velocity due to friction (υ_f). Expanding Equation (2.3), so we get

$$F_{tot} = c(\upsilon + \upsilon_f) \tag{2.4}$$

which includes the effective friction term into the model. Afterwards with the assumption of damping and friction arise from the droplet perimeter, it is scalable with the diameter (d). Combination of Equation (2.2) and (2.4) results the relation between droplet velocity and temperature

$$\upsilon \sim m\alpha(T - T_c)^2 - v_f \tag{2.5}$$

where m is the mobility or the inverse damping coefficient (1/ c). The Ga droplet velocity becomes zero when $(T - T_c)^2 < v_f/(m\alpha)$. From Equation (2.5), we may also conclude that the velocity of Ga droplets is proportional to $(T - T_c)^2$. As the $(T - T_c)^2$ term rises, the droplet velocity will also increase.

Figure 2.5 shows the experimental result clarifying Equation (2.5). T_c is in between 615 °C and 635 °C where droplets immobile in this temperature range. Above and below T_c, we have seen the non-zero droplet velocity, which indicates that the motion of Ga droplets occurs not only above T_c, but also below T_c as shown in Figure 2.5(b). However, to get mobile droplet at temperature below T_c, the temperature must first increases above T_c to create a Ga-rich surface and allow the Ga droplet formation. In addition, during running, the droplet size is seen to grow above T_c and shrink below T_c as shown in Figure 2.5(a).

2.4 Running Droplet Dynamics

This part explains the dynamics of running droplets. Of particular interests are the running trails [6], the critical size of the droplets [5], secondary droplets [22], and coalescence events [23].

2.4.1 Running Trails and Critical Size

The running droplet trails are shown in Figure 2.6. The trails noticeably in the form of nano-terraces as a result of the stick-slip motion of Ga droplets. The stick-slip motion of Ga droplets is a periodic local etching interaction between Ga droplets and GaAs (001) surface. As reported by Hilner et al [12], Ga droplets motion is associated with the surface morphology of surface in front of the droplets. During the slip state, the droplets move to rougher areas; the surface friction increases due to the buried areas. With the increase in friction, the droplets reach the stick state until reaching the ordering of crystal structure underneath. After that, the droplets return to the slip state and move to the newer rough areas. This process happens periodically, creating stick-slip motion and the observation of running trails as shown in Figure 2.6.

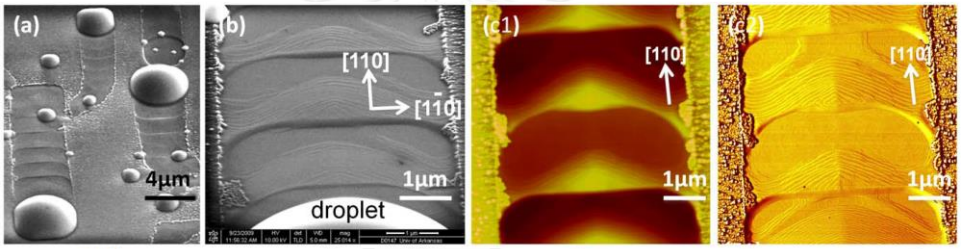

Figure 2.6 Nano terraces running trails as a result of stick-slip motion of Ga droplets on GaAs (001) [6].

In addition, to be mobile, the droplet must reach a critical size because F_{tot} is categorized as a size-dependant parameter; the bigger the droplets, the higher the total force vector or F_{tot}. At a sublimation temperature of 680 °C, Wu et al. [5] observed Ga droplets start to move after reaching an average critical diameter of 1.9 μm.

2.4.2 Secondary Droplets

Figure 2.7 shows the observation of secondary droplet which exists because of the non-uniform evaporation rate along the primary droplet running trails. The high evaporation rate in the edge of primary running trail induces the formation of secondary droplet. The secondary droplet which has a diameter less than 0.5 μm will remain on the edge of trail as shown in Figure 2.7(a). Over time, the secondary droplet is growing up, until the secondary droplet reach diameter 0.5 μm; they will

start to move away from the primary droplets trail along [1-10] crystal orientation as shown in Figures 2.7(b) and 2.7(c). Afterwards when the size of secondary droplet reaches a diameter of about 2 μm, they behave like a primary droplet, turning into [110] as shown in Figure 2.7(d).

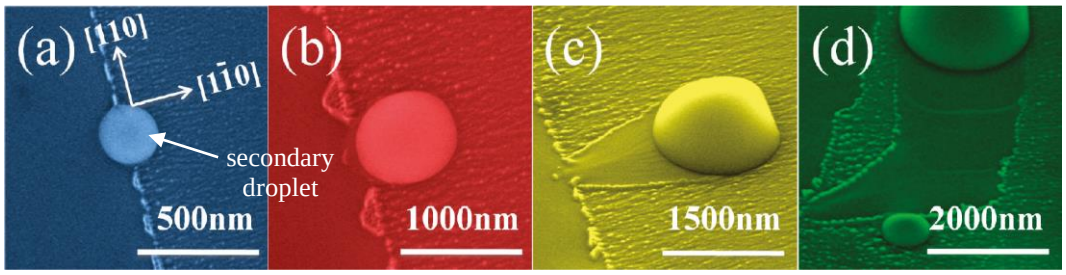

Figure 2.7 The evolution of secondary droplet during self-running Ga droplets on GaAs (001) [22].

2.4.3 Droplets Wettability and Coalescence

Two last droplet dynamics are the droplets wettability and coalescence event. Wettability is the tendency of liquid droplets to conserve contact with a solid surface. Wettability is characterized by adhesive and cohesive forces between droplets and solid surface; adhesive and cohesive forces cause droplets to spread along the surface and evolve up (avoiding contact with surface), respectively. A liquid droplet spreading on the surface without absorption of droplet by the surface is known as inert/ non-reactive wetting. On the other hand, a liquid droplet influenced with absorption by the surface is known as reactive wetting. Droplet in semiconductor is the reactive wetting system which affects droplet coalescence dynamic.

Figure 2.8(a) demonstrates the coalescence of two droplets in non-reactive system while the force balance of a single non-reactive droplet is shown in (b). The mathematical model of corresponding single non-reactive droplet follows Young's equation as given in Equation (2.6):

$$\gamma_{vs} - \gamma_{ls} = \gamma_{vl} \cos\theta \tag{2.6}$$

where γ_{vs}, γ_{ls}, and γ_{vl} are the surface tensions of vapor-solid, liquid-solid, and vapor-liquid interface, respectively. The contact angle, θ, will be reduced during the collision state since the centre of mass are moving to the neck region.

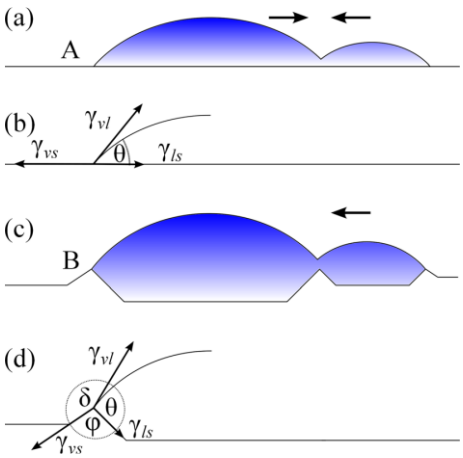

Figure 2.8 The models compare the droplet coalescence of non-reactive system (a, b) and the Ga droplets during self-running Ga droplets on GaAs (001) (c, d) [23].

Figure 2.8(c) illustrates the coalescence of two droplets in reactive system while the force balance of a single reactive droplet is shown in Figure 2.8(d). The mathematical model of a single reactive droplet follows the Young's equation with a small modification. Introducing new contact angles, δ and φ, the force equilibriums are not only in the horizontal but also in the vertical. Using Neumann's triangle method [24], it can be shown that the relations between surface tensions and the three contact angles are

$$\gamma_{vs} + \gamma_{ls}\cos\varphi + \gamma_{vl}\cos\delta = 0 \tag{2.7}$$

$$\gamma_{vs}\cos\varphi + \gamma_{ls} + \gamma_{vl}\cos\theta = 0 \tag{2.8}$$

$$\gamma_{vs}\cos\delta + \gamma_{ls}\cos\theta + \gamma_{vl} = 0 \tag{2.9}$$

where $\theta + \varphi + \delta$ is 2π. Then, deriving three homogenous equations of surface tensions vs contact angles, Equations (2.7 – 2.9), the ratio of tensions depends only on the ratio of contact angles as

$$\frac{\gamma_{vs}}{\sin\theta} = \frac{\gamma_{vl}}{\sin\varphi} = \frac{\gamma_{ls}}{\sin\delta} \tag{2.10}$$

In addition, the bigger droplet intends to absorb the small droplet, because the center of mass during the coalescence event is located in the center of the larger of the two droplets.

2.5 Running Droplets on Various Semiconductor Surfaces

Recent studies discover that the running droplets occur not only on GaAs (001) but also on various surfaces: GaAs (111)A and B [13], InP [25], InAs and InSb [26, 27].

2.5.1 Ga Droplets on GaAs (111)A and (111)B

Running droplets on GaAs (111)B are similar to those on GaAs (001). The major different is that the GaAs (001) have a higher T_c than the GaAs (111)B, resulting the droplets speed on the GaAs (001) slower than those on the GaAs (111)B in accordance with Equation (2.5).

For (111)A, the droplets nucleation and trail profiles are very different from GaAs (111)B and (001) due to the etching nature of zincblende semiconductors [28, 29]. In zincblende semiconductors, under thermal and chemical etchings, the droplet base is inverted pyramid as a result of etched edge dislocation lines. The droplet base shape influences the droplets nucleation and the running trail as shown in Figure 2.9.

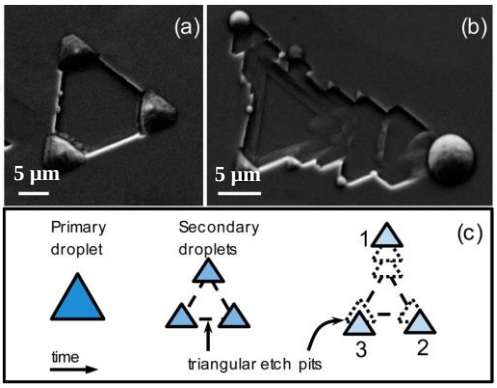

Figure 2.9 The schematic of droplets nucleation and triangular running trails on GaAs (111)A [13].

Figure 2.9(c) shows the schematic diagram of Ga droplets nucleation and running on GaAs (111)A. After nucleation, the primary droplet breaks up into three secondary droplets as observed from post-annealed SEM image in Figure 2.9(a). In the early

stage of the secondary droplets running, the running directions are partially guided by the edge dislocations; they move away from primary etch pit in the normal side direction, producing triangular trails due to the inverted pyramid downward etching and the forward motion of Ga droplet. The droplet shapes also cycle between triangular and circular during stick-slip motion.

2.5.2 In Droplets on InAs (111)B and InP

Apart from running Ga droplets, running In droplets on InAs (111)B and InP have been reported by Mandl et al. [27] and Kanjanachuchai et al. [25], respectively. Mandl et al show the Langmuir evaporation of InAs (111)B with and without SiO_x layer. The result showed that the running In droplets only occur on the clean surface (InAs (111)B without SiO_x layer) as shown in Figure 2.9. There is not much information that can be elaborated from this experiments, until Kanjanachuchai et al. reported running In droplets on three different planes of InP: the (001), (111)A and B which qualitatively explains the running In droplets dynamics.

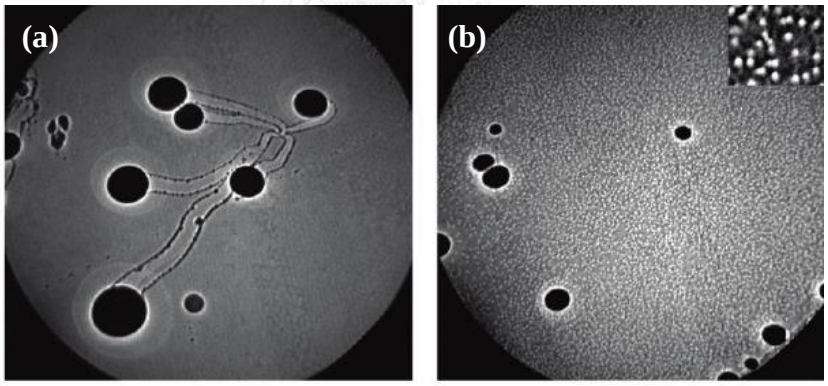

Figure 2.10 LEEM images showing (a) running In droplets on InAs (111)B without SiO_x layer and (b) immobile In droplets on InAs (111)B with SiO_x layer underneath [27].

Figure 2.11 shows time-lapse captured LEEM images of running In droplets on InP (001), (111)A and B. From the three different planes observations, running In droplets share one similarity: they are breakup before start to move.

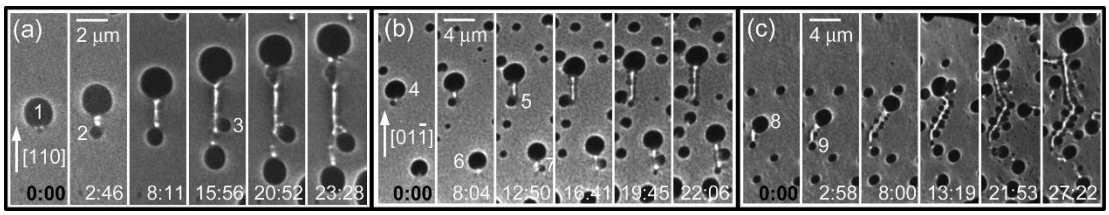

Figure 2.11 Time-lapse LEEM images showing breakup behaviour of running In droplets on InP (a) (001), (b) (111)A, and (c) (111)B surfaces [25].

This can be explained through a spreading liquid droplet on a solid surface [30] Equation as

$$F_v = \frac{\mu U R}{h_d} \tag{2.11}$$

where F_v is the viscos force, μ is the droplet's viscosity, R is the droplet base radius, U is the contact line velocity or dR/dt, and h_d is the droplet height. Equation (2.11) shows that the viscos force F_v, the force that counteracted the droplet spreading force, is proportional to the droplet's viscosity μ. Hence, the higher the μ, the more the tendency of droplet to spread on the surface. μ is temperature-dependant that can be approximated by

$$\log_{10}(\mu/\mu^0) = -a_1 + \frac{a_2}{T} \tag{2.12}$$

where μ^0 is 1 mPa s, T is the absolute temperature (K), a_1 (-) and a_2 (K) is the coefficients from the reference viscosity table [31]. We can compare μ of the In and the Ga droplets, to understand the origin of the In droplets breaking up characteristics. Putting the active temperature T_A of InP (001) and GaAs (001) where the droplets are mobile into Equation (2.12), T_A (μ) are approximated to be 369 ºC (1.15 mPa s) and 630 ºC (0.60 mPa s) for the In and the Ga droplets, respectively. In droplets receive about two times greater μ than Ga droplets, resulting In droplets more sticky and easily to break up than Ga droplets.

Besides the breaking up characteristics, the running directions of In droplets in three different planes are also interesting to explore. Figure 2.12 shows the SEM images of post-annealed InP (001), (111)A, and (111)B. For InP (001), the directions of running In droplets are similar to the running Ga droplets on GaAs (001). The primary In droplets, marked as m in Figure 2.12(a), run toward [110] or [-1-10] with approximately equal probabilities; from the trail's path of the secondary In droplet, marked as n in Figure 2.12(a), the secondary In droplet that reaches a critical diameter will run away along [1-10], and overtime they make a turning to [110] or [-1-10]. The commonalities between the InP (001) and the GaAs (001) suggest that the driving force on both systems are from the similar origin i.e., the surface chemical potential.

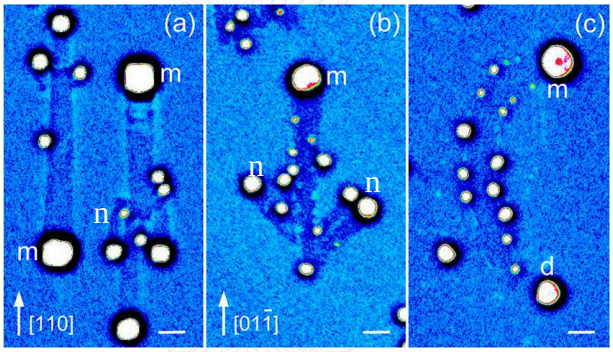

Figure 2.12 Re-colored SEM images exhibiting running In droplets on InP (a) (001), (b) (111)A, and (c) (111)B. The scale bars are 2 μm [25].

The In (111)A droplets characteristic is much different from the Ga (111)A droplets. The observation of triangular pits on GaAs (111)A vanishes on the InP (111)A. The mobile In (111)A droplets are circular and start to move at a critical diameter of 0.7 μm, similar to those in the In (001) [25]. The primary In (111)A droplets move along [01-1] direction, as shown in Figure 2.12(b), marked as m, following with the secondary In (111)A droplets formation on the edge of trail due to the non-uniformities of evaporation rate. The secondary In (111)A droplets, marked as n, are seen to move out from the trail at approximately 45º from the [01-1].

The In (111)B droplets are seen to move in a random direction as shown in Figure 2.12(c), marked as m. The droplet revolves for more than 10 μm, possibly due to the imbalance of the droplet's forces direction. Two droplet's forces responsible for the directionality of droplets are called a diffusion force along diffusion barrier

orientation (F_{diff}) and a drift force resulted from spatial variation of $\Delta\mu$ (F_{drift}) as illustrated in Figure 2.13.

In an immobile droplet, Figure 2.13(a), surrounded by the uniform surfaces, resulting the neutralization of F_{drift}. While in a mobile droplet surrounded by the chemically-, thermally-, or otherwise-induced non-uniform surfaces, causing the magnitude of F_{drift} is greater than F_{diff}. Then as illustrated in Figure 2.13(b), the mobile droplet moves toward the direction of the maximum force F_m (shown as dashed red arrows).

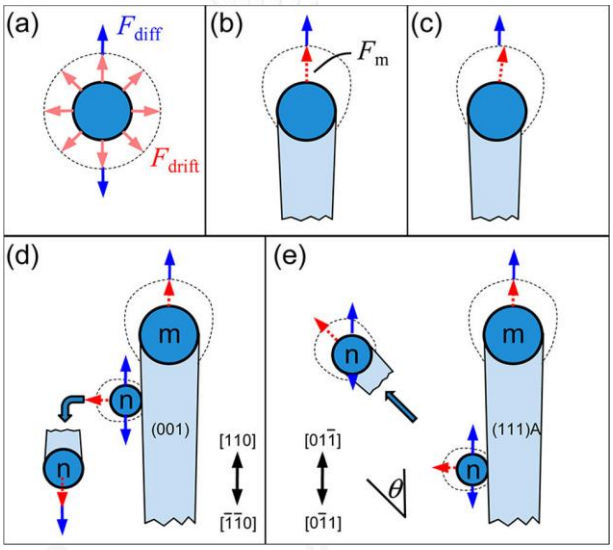

Figure 2.13 The models showing the roles of a diffusion related force (F_{diff}) and a drift related force (F_{drift}) on In droplets that (a) immobile and mobile: (b) straight, (c) nonstraight, (d) on InP (001), and (e) on InP 111(A) [25].

For In (111)B, as illustrated in Figure 2.13(c), the directionless motion may be caused by the magnitude of F_{diff} (shown as solid blue arrows) much smaller than F_m. But F_{diff} is dominant on primary In droplets (marked as m in Figure 2.13) for In (001) and (111)A, causing the motion along diffusion barrier direction.

For the secondary In droplets directions (marked as n in Figure 2.13) are different between InAs (001) and (111)A. In figure 2.13(d), secondary In (001)

droplet is seen to move perpendicular from the primary droplet trail and to turn into diffusion barrier direction [-1-10], possibly because F_{diff} is stronger than F_m. In contrary, in figure 2.13(e), secondary In (111)A droplet are observed to move 45º away from the primary droplet trail, indicating that $\| F_{diff} \| \approx \| F_m \|$.

2.5.3 In Droplets on InAs and InSb (111)B

The running characteristics of In droplets vary widely amongst the different systems i.e., In droplets on InP, InAs (111)B, and InSb (111)B. The breaking up behaviour of In droplets on InP is absent in InAs (111)B. In droplets on InSb (111)B also exhibit different characteristic; they nucleate in the triangular pits similar to Ga (111)A droplets. Even in the same system, InAs (111)B, the different Langmuir evaporation preparations may result in the different droplets characteristic: the directionless motion and the motion toward [-12-1] of In (111)B droplets are generated from a fast ramping annealing [27] and a very slow ramping annealing [26], respectively.

Other important of droplets despite the running characteristics, is the running controls. The running controls of the metallic droplets on the semiconductor surfaces (reactive droplets) are relatively new design and the creations are more complicated due to the reactive wetting system as explained in Section 2.4.3. While on their counterparts, the liquid droplets on the solid surfaces (nonreactive droplets), the running controls are already established that consist mainly of the droplet's speed and direction controls, achieved by creating a resource of controller e.g., magnetic fields [32], lateral vibration [33], gravity [34], and thermal gradient [35]. However, Kanjanachuchai et al. [26] recently proposed a method using a dislocation network for guiding the direction of running reactive droplets.

From the Langmuir evaporation of an unintentionally stressing InAs (111)B, the direction control of droplets is obtained by two scenarios: a single (shown in Figure 2.14(a)) and multiples (shown in Figures 2.14(b) and 2.14(c)) of line dislocation-droplet interaction. In Figure 2.14(a), the line dislocation, marked as L1, fully guides the first droplet, marked as D1, to run toward [10-1]. Although not all droplets can be guided by L1; the second droplet, marked as D2, is partially guided by

L1. During guided-running, the droplet D2 runs toward [10-1] and gains momentum, and then after achieving critical momentum, it turn into [-12-1], the majority direction of droplets.

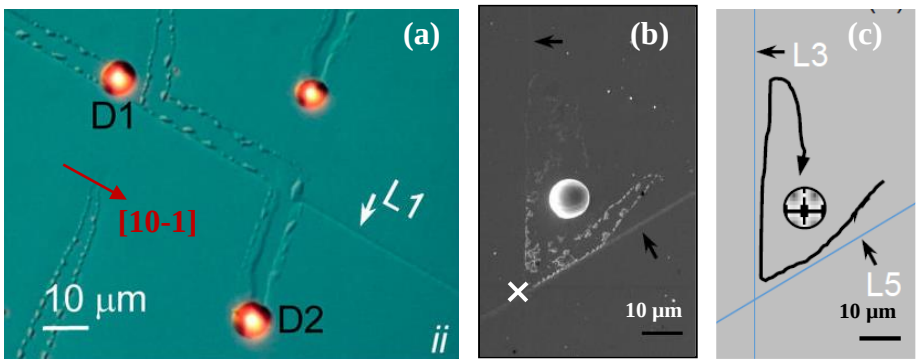

Figure 2.14 (a) DIC image showing a single line dislocation and In droplets interaction (b) SEM image showing multiples line dislocations and an In droplet interaction (c) trajectory of a guided In droplet on the post-sublimated InAs (111)B surface [26].

Figures 2.14(b) and 2.14(c) show the interaction between multiple line dislocations (marked as L3 and L5) and a single In (111)B droplet. These two line dislocations are seen as effective guidance, blocking the droplet to run across the intersection, marked as multiplication (x) sign in Figure 2.14(b).

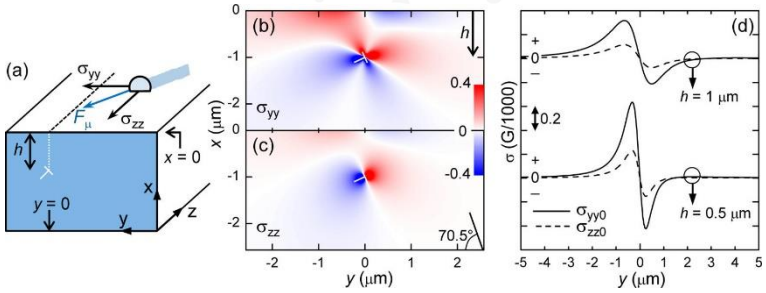

Figure 2.15 (a) The model showing a running liquid droplet approaches a dislocation line buried at depth *h*. Simulated cross-sectional stress distribution of (b) σ_{yy}, (c) σ_{zz} at y = 0 and x = -1 (d) simulated surface stress distribution for h = 1 μm and h = 0.5 μm [26].

The droplet-dislocation line interaction can be modelled using Eshelby's technique for determining the stress and strain in the buried dislocation, as previously used by Andrews et al. [36] for modelling the cross-hatch strain fields. A running

droplet with running force F_μ approaches a dislocation line and experiences a local force F_σ as shown in Figure 2.15(a). F_σ occurs due to the surface stress σ from buried dislocation line which is composed by the perpendicular (σ_{yy}) and the parallel (σ_{yzz}) components.

The surface stress components can be calculated by considering the pure edge dislocation as

$$\boldsymbol{b} = b_x\boldsymbol{e}_x + b_y\boldsymbol{e}_y \tag{2.13}$$

where b is the Burger vector, $\mathbf{e}_x$ is the x unit vector, and $\mathbf{e}_y$ is the y unit vector. While the mathematical expressions for the surface stress tensor of any position (x,y) are [36]

$$\sigma_{yy}^{b_x} = \frac{Gb_x}{2\pi(1-v)}\left\{\frac{y[(x+h)^2-y^2]}{[(x+h)^2+y^2]^2} + \frac{y(7h^2-6hx-x^2+y^2)}{[(x-h)^2+y^2]^2} + 4xyh\frac{3(x-h)^2-y^2}{[(x-h)^2+y^2]^3}\right\} \tag{2.14}$$

$$\sigma_{yy}^{b_y} = \frac{Gb_y}{2\pi(1-v)}\left\{\frac{(x+h)[(x+h)^2+y^2]}{[(x+h)^2+y^2]^2} - \frac{h^3+h^2x-5h(x^2+y^2)+x(3x^2+y^2)}{[(x-h)^2+y^2]^2} - 2x\frac{h^4-2h^3x-x^4-6h^2y^2+y^4+2h(x^3+3xy^2)}{[(x-h)^2+y^2]^3}\right\} \tag{2.15}$$

$$\sigma_{zz}^{b_x} = \frac{Gb_xv}{2\pi(1-v)}\left\{\frac{2y(5h^2-6hx+x^2+y^2)}{[(x-h)^2+y^2]^2} - \frac{2y}{[(x+h)^2+y^2]^2}\right\} \tag{2.16}$$

and, $$\sigma_{zz}^{b_y} = \frac{Gb_yv}{2\pi(1-v)}\left\{\frac{2(x+h)}{[(x+h)^2+y^2]} - \frac{2[h^3-h^2x+x(x^2+y^2)-h(x^2+3y^2)]}{[(x-h)^2+y^2]^2}\right\} \tag{2.17}$$

where the shear modulus *G* and the Poisson's ratio *v* are the coefficients of the elastic isotropic solid medium e.g., in room temperature, *v* for InAs (111) is 0.362 [37]. The burger vector, used for simulation in Figures 2.15(b), 2.15(c), and 2.15(d) is

$$\boldsymbol{b} = \left(\frac{2\sqrt{2}}{3}\right) b\boldsymbol{e}_x + \frac{1}{3}b\boldsymbol{e}_y \tag{2.18}$$

according to the 70.5º intersection angle between a {111}c slip plane and the InAs (111) surface. The simulations in Figures 2.15(b), 2.15(c), and 2.15(d) are then generated, showing the surface and the cross-sectional stress distributions of the InAs (111) where the numerical σ values are in the unit of 10^{-3}G.

The simulation results show that the degree of droplet and dislocation (F_μ and F_σ) interaction relies on the surface step Δx which mean relies also on the depth of buried dislocation h. Figure 2.15(d) shows the surface stress σ distribution for h = 1 μm and h = 0.5 μm where σ falls on maximum value at y = 0, and then decreases to zero for further areas. Wherein the reduced h results in the increasing of σ (and the corresponding force F_σ) and the decreasing of influenced range.

The running characteristics of reactive droplets on the buried dislocation surface can be qualitatively explained. When the droplets at areas far away from dislocation; they will run toward the majority direction because the only dominant force is F_μ, regardless of F_σ. F_σ appears within a distance of y<2h-3h, which are close enough from the dislocation. Upon the appearing of F_σ, the direction of running droplets follows the vector sum of F_μ and F_σ.

F_μ is proportional to droplet diameter d according to Equation (2.2), whereas F_σ is inversely proportional to h, so that the droplet-dislocation interactions are summarized as follows: (1) small droplets, having a low F_μ, approach shallow dislocations (high F_σ) are fully guided by the dislocation since the droplets do not have enough energy to run accros the dislocation (barrier). (2) small droplets approach deep dislocations (low F_σ) are partially guided (deflected slighlty) or even cross over the barrier. (3) Big droplets, having a high F_μ, approach deep dislocations will cross over the dislocation because F_μ is much greater than F_σ. The last, (4) Big droplets approach shallow dislocations possibly be fully guided or cross over the barrier [26].

2.6 InGaAs Cross-Hatch Patterns as Guiding Layer

One of the objectives of this thesis is controlled manipulation of droplets direction using cross-hatch patterns (CHPs). CHPs have been used for various templates e.g., nanoholes [38] and quantum dots [39, 40], while in this thesis CHPs are used as template for guiding running Ga droplets.

Similar to the dislocations on InAs (111)B by stressing sample at high temperatures [26, 28] which is described in Section 2.5.3, CHPs also consist of buried dislocations, regardless of the formation by heteroepitaxy and the readily known properties [41, 42]. This part explains the theory and the characteristics underlying the

dislocations formation of CHPs, while the cross-sectional and the growth details of this structure are presented in Section 3.1.5.

CHPs are formed due to strain relaxation, similar to QDs: the nature of the two crystals with different lattice constant coupling [43]. However, to grow CHPs instead of QDs, the degree of mismatch (strain) ε must to be low (<2%) [44]. ε is calculated by

$$\varepsilon = \frac{a - a_0}{a_0} \tag{2.18}$$

where a is the lattice constant of strained layer and a_0 is the lattice constant of unstrained layer (substrate) [45]. Three growth modes are obtained from the different ε and the layer thickness (H): Frank-van de Merwe (FM), Stranski-Krastanov (SK), and Volmer-Weber (VW) [46]. The FM mode is a 2 dimensional (2D) layer-by-layer growth where the mismatch ε is less than 10%, whilst the SK mode is a 3 dimensional (3D) growth where ε is in between 5% and 15%. However, in SK mode, there is still possible to grow a 2D structures the so-called wetting layer (WL) before the 3D structures occur at H above the critical value (H_c). For the VW mode, ε is sufficiently high to make the formation of 3D structures without the WL.

Figure 2.16 shows the schematic diagram of CHPs formation. For the growth of CHPs, ε is mantained in the mode ranges of 2D layer-by-layer growth using the FM mode [40]. The heteroepitaxy growth of two slightly lattice-mismatched crystals (strained layer and substrate) results in the point defect due to the missing row of atomic ordering. When the strained layer thickness exceeds H_c, the strain relaxation occurs, after that misfit dislocations (MDs) will form. The further growth of strained layer increases the strain energy and creates the propagating of dislocation toward the strained layer surface, creating the surface step or cross-hatch patterns in the atomic force microscope representation [41, 44].

The well-known CHPs formation is in the heteroepitaxy of $In_xGa_{1-x}As$ on flat (001) GaAs surface, where x is the In molar fraction. For this thesis, the CHPs that is used as guiding layer for running droplets is $In_{0.2}Ga_{0.8}As$/GaAs with the strained layer thickness of 25 nm. Since the mismatch ε between $In_{0.2}Ga_{0.8}As$ and GaAs is 1.4% [47], below 2%, the growth occurs in the 2D layer-by-layer mode. The strain between the

two structures is relaxed by the formation of 60° MDs, resulting in the formation of CHPs along [110] and [-110] directions.

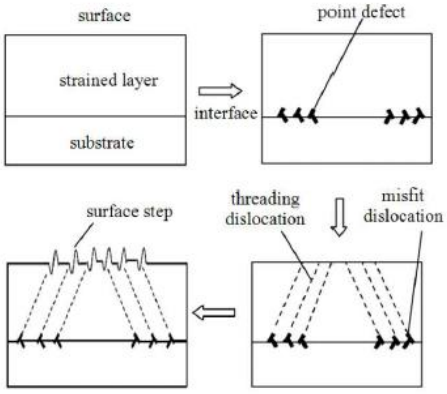

Figure 2.16 The schematic diagram showing the formation of CHPs [44].

Figure 2.17 shows ECCI image and linescans of a 25 nm $In_{0.2}Ga_{0.8}As$ grown on GaAs (001) surface. Surface steps (undulations) of CHPs serve as a guidance to manipulate running droplets direction. The magnitude of undulation lines along [110] and [-110] is observed to be 1 μm, which is sufficient to interact with droplet that tipically etch about 100 nm of the GaAs surface [6].

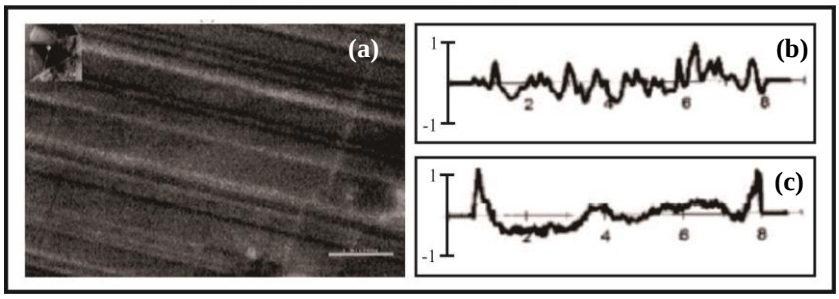

Figure 2.17 (a) Electron channelling contrast imaging (ECCI) of a 25 nm $In_{0.2}Ga_{0.8}As$. ECCI linescans of a 25 nm $In_{0.2}Ga_{0.8}As$, taken across the (b) [110] and (c) [-110]. The axes scales of b and c are in μm [42].

2.7 Metal-Semiconductor (MS) Junction

Droplet on semiconductor surface is a metal-semiconductor (MS) junction which characteristics are similar to the characteristics of p–n diode, light emitting diode (LED), and solar cells. The MS junction can be either rectifying or non-

rectifying. The rectifying forms a Schottky barrier and the non-rectifying forms an ohmic contact.

The classification of MS junction to be a Schottky barrier or an ohmic contact depend on the Schottky barrier height Φ_B. When Φ_B is sufficiently higher than the thermal energy k_BT, the semiconductor bends near the metal, and the MS junction behaves as Schottky barrier. Whereas in a lower Φ_B, the semiconductor is not bends, and the MS junction behaves as ohmic contact.

Figure 2.18 shows a band diagram of n-type Schottky diode, where Φ_{B0} is the ideal barrier height, V_{bi} is the built-in voltage, E_c is the conduction band, E_v is the valence band, E_f is the Fermi level, and E_{fi} is the intrinsic Fermi level. In the semiconductor region, the band bends downward and the conduction band is closer to the Fermi level because the metal and the semiconductor share the equilibrium level. The work function—the minimum energy required to remove an electron from the surface—of the metal is higher than that of the semiconductor. Therefore, before equilibrium, the electron flows from the semiconductor to the metal, increasing the the built-in potential of the semiconductor.

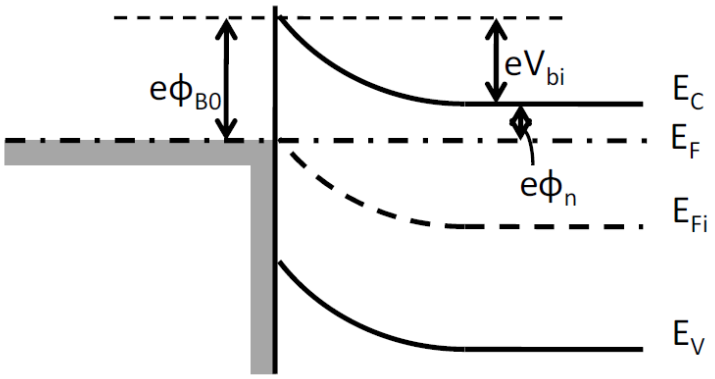

Figure 2.18 Energy band diagram of an n-type Schottky diode, adapted from Neamen, D.A. and B. Pevzner [48]

The Schottky barrier height Φ_B can be obtained from current-voltage (*I*-*V*) and capacitance-voltage (*C*-*V*) methods with an assumption of homogeneous system [49]. For an *I*-*V* method, the junction current *I* is measured as a function of the applied bias voltage V_b and the relation is

$$I = I_{sat}\left[\exp\left(\frac{qV_b}{nkT}\right)-1\right] \tag{2.19}$$

and the reverse saturation current I_{sat} is

$$I_{sat} = AA^{*}T^{2}\exp[-\Phi^{0}{}_{B,n}/(k_BT)] \tag{2.20}$$

where A is the junction area, A^* is the Richardson's constant, and T is temperature. I_{sat} and the ideality factor n can be calculated from the semi-logarithmic plot of V_b vs dark current I_{dark}. Dark I-V measurement ensures the absent of series and shunt resistances [50]. The ideality factor measures the closeness of a device characteristics to the ideal diode. The ideality factor is also a powerful indicator to describe the recombination in a device. For an ideal device (n=1), the recombination occurs by band-to-band recombination, but for a non-ideal device (n=2), the recombination occurs by defects in the depletion region. In a real device, both recombinations take place, so typical values of the ideality factor are between 1 and 2 [51].

For C-V method, the junction capacitance C (typically ≈ 100kHz) is measured as a function of V_b. The measurement is conducted in reverse bias for reducing the influence of in-phase current. After plotting the inverse of C vs V_b, flat-band voltage is calculated by a linear extrapolation to the voltage axis. Φ_B of an n-type MS is

$$\Phi^{0}{}_{B,n} = eV_{bi} + eV_n + k_BT \tag{2.21}$$

where eV_{bi} is the built-in voltage and eV_n is the difference between the conduction band E_c and fermi energy E_f level of the semiconductor [52].

CHAPTER 3
Experimental Details

This chapter explains the details of samples fabrication and characterization which are divided into 6 Sections. Section 3.1 explains about molecular beam epitaxy (MBE) experiments. Section 3.2 presents about reflection high-electron energy diffraction (RHEED) observation for the surface reconstruction. Section 3.3 explains about a low-energy electron microscopy (LEEM). Section 3.4 explains the details of e*x situ* analyses using differential interference contrast (DIC) microscopy, atomic force microscopy (AFM), and scanning electron microscopy (SEM). Section 3.5 presents about the selective Ga droplets etching by a chemical solution. Finally, Section 3.6 explains about sharp tungsten (W) tip fabrication and droplet *I-V* characterization.

3.1 Molecular Beam Epitaxy (MBE) Experiments

3.1.1 The MBE Machine

Just as the name suggests MBE is a type of epitaxial crystal growth using beams of elements. The word epitaxy is adopted from Greek word *epis* and *taxis*, which mean to *over* and *order*, respectively. Thus, MBE is the growth of an *ordered* layer *over* another existing layer or the so-called deposition, using beams of elements. However, in this thesis, the works use MBE not for deposition growth but for decomposition growth.

All samples were sublimated using Riber's 32P solid-source MBE. This machine is equipped with three chambers: introduction, transfer and growth chamber. Figure 3.1(a) shows the MBE's growth chamber sketch. Effusion cells with the pure of group III and V materials (In, Al, Ga, P, and As_4) produce the molecular beams. The molecular beams are generated by evaporating the materials under UHV which the temperatures controlled by feedback from thermocouples reading. The UHV creates the mean free path of beams very smooth with allow the beams to reach the sample surface with minimum collisions. Flux of the beams towards the sample surface can be turned on/ off by controlling the tantalum shutters in front of the cells.

The beam flux rates as a function of cell temperatures are calibrated using RHEED. RHEED also play important roles as surface reconstruction tool distinguishing between flat and rough surfaces. RHEED imaging system consists of an electron gun, a fluorescent screen, and a CCD camera connected to a computer.

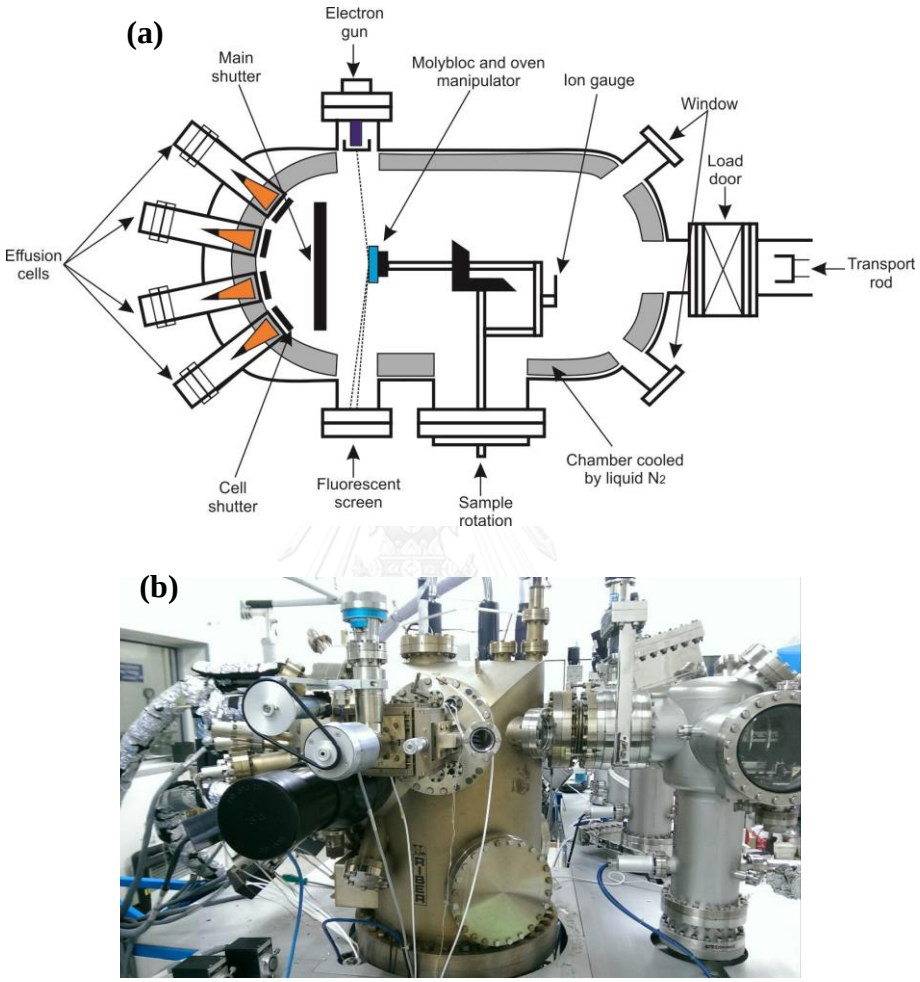

Figure 3.1 (a) Top-view sketch of Riber's 32P growth chamber (b) Side-view picture of Chulalongkorn's MBE growth chamber.

3.1.2 Samples Preparation

All samples are scribed from epi-ready GaAs (001) substrates and are attached to molybloc using indium (In) glue. Afterwards, the sample is loaded to introduction chamber and baked at 450 °C for one hour under UHV to get rid of the water (H_2O) contamination. The sample then transferred to growth chamber and additional baking made at 580 °C to desorb the oxide layer.

3.1.3 Producing Self-Running Ga Droplets

MBE is not designed for microscopy; RHEED patterns which lack of real-space imaging capability, leading to under- or over-decomposition and make it difficult to get running Ga droplets. Moreover, in our observations, there is no information of RHEED pattern for running droplets due to RHEED pattern disappearance because of the μm size of droplets that absorb, scatter, or reflect the electron beam from the RHEED gun. To solve the inability to see surface condition in MBE, Jesson et al. [53] proposed a method by installing III-V source cells on low-energy electron microscopy (LEEM); they also can reproduce running droplets in this machine. However, we also found a simple applicable procedure in common MBE for producing running Ga droplets. In this procedure, primary surface indicator is RHEED and rough sample temperature indicator uses thermocouple reading. The procedure establishment requires six samples as shown in Figure 3.2.

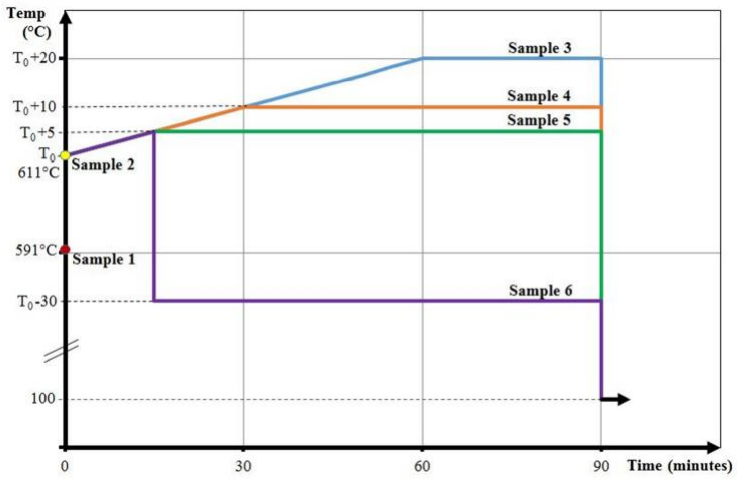

Figure 3.2 Temperature profiles of samples used for establishing self-running Ga droplets procedure in MBE.

Starting from ramping up the temperature from 100 °C to 580 °C with a rate of 30 °C/ min. Sequentially, in the temperature range between 580 °C and until the first appearance of streaky patterns (where the progress stops for sample 1), the ramping up rate decreases to 10 °C/ min. The temperature stops at streaky pattern for 30 min, to allow oxides desorption process. After that, the temperature increases with a rate of 1 °C/ min until the streaky patterns turn into chevron patterns (where the progress

stops for sample 2). In addition, the PID program of temperature is halted when the system pressure exceeds 5.5 x 10^{-9} Torr. After quenching samples 1 and 2, the surfaces are analyzed *ex situ* using AFM.

Reproducible running Ga droplets can be formed in MBE by registering RHEED chevron patterns and applying profiles with corrected temperature. The temperature T_0 indicates where the chevron pattern appears, and was then used in samples 3-6 as the reference temperature. Temperature of sample 3 is ramped from T_0 to T_0 + 20 °C at a rate of 0.3 °C/min and then sublimated for 30 min. This slow ramping rate was used for all samples to avoid quick decomposition and alllows density control [25]. Temperature of samples 4 and 5 are ramped from T_0 to T_0 + 10 °C and T_0 + 5 °C and then sublimated for 60 and 90 min, respectively. Temperature of sample 6 at first rises to T_0 + 5 °C, to make a Ga-rich surface that allows Ga droplets nucleation, afterwards it directly decline to T_0 – 30 °C and maintained constant for 75 min. After each sublimation, the temperature decreases 100 °C by switching off the power supply of heater. Samples 3-6 are analyzed *ex situ* using an AFM, a differential interference contrast (DIC) microscopy, and a scanning electron microscopy (SEM).

3.1.4 Samples for Selective Ga Droplets Etching and Droplet *I-V* Characterization

Before obtaining the procedure to reproducible produces running Ga droplets in MBE as explained in Section 3.1.3, we got many over-decomposition samples: the surface is dominated by large size-droplets without running trails.

The over-decomposition samples can be used for selective Ga droplet etching and droplet *I-V* characterizations. Selective Ga droplets etching is used to determine the etch pit geometry underneath the droplet and to ensure the formation of Ga droplet. While the droplet *I-V* characterization is used to acquire the electrical properties of droplet—a droplet on semiconductor surface may have some similarities to a diode.

These experiments use samples 7 and 8: the chemical solution testing of selective Ga droplets etching uses sample 7 while samples 8 is used for droplet *I-V* characterization because the droplets are big enough to be probed by sharp tungsten (W) tip.

Samples 7 and 8 are sublimated with the following procedure. The ramping up temperature from 100 °C until the thermal oxide desorption temperature of these samples is similar to those of samples 1-6. After 10 min of thermal oxide desorption, the temperature of samples increases to the sublimation temperature. For sample 7, the temperature increases to 680 at a rate of 5 °C/ min and kept constant for 10 min. For sample 8, the temperature increases to 680 °C at a rate of 1 °C/ min and kept constant for 10 min.

3.1.5 Samples for Manipulation of Self-Running Ga Droplets Migration using CHPs

Figure 3.3 shows the schematic diagram of samples in this experiment. A GaAs sacrificed layer with thickness *i* is grown on top of an $In_{0.2}Ga_{0.8}As$ CHPs layer. Samples 9 and 10 with *i* of 100 nm and 300 nm, respectively, were grown. The detailed steps for samples growth are as follows. After 10 min of oxide desorption, a 100 nm buffer layer is grown to flatten the surface using a growth rate of 0.6 ML/s at 580 °C. After that, the substrate temperature is ramped down to 500 °C and a 25 nm $In_{0.2}Ga_{0.8}As$ is grown as guiding layer for running droplets. Subsequently, a 20 seconds growth interruption and a GaAs sacrificed layer growth for respective *i* were carried out. After the growth process, the system pressure is above 5 x 10^{-9} Torr—too high for performing sublimation—substrate temperature then decreased to 100 °C by switching off the power supply of heater and the sample is transferred to the introduction chamber.

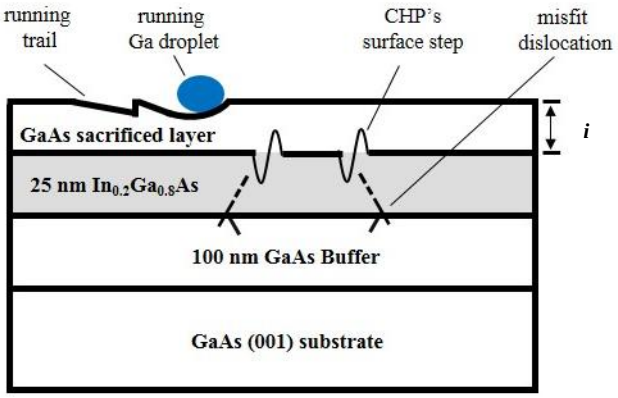

Figure 3.3 Cross-sectional schematic diagram of running Ga droplets on cross-hatch patterns.

On the next day, the pressure decreases below 5 x 10^{-9} Torr; the sample is returned back to the growth chamber and the sublimation is performed. Samples 9 and 10 are sublimated in MBE with the following procedure. Sample 9 is sublimated at 685 °C for 10 min by ramping the temperature from 100 °C to 685 °C at a rate of 5 °C/ min. Sample 10 is sublimated at 695 °C for 10 min by ramping the temperature from 100 °C to 695 °C at a rate of 4 °C/ min. In both samples, we cannot find the chevron patterns—which always found in samples 1 to 6—the droplets formation is estimated through the dissappearing of RHEED patterns. After each sublimation, the temperature of these samples are cooled down to 100 °C by switching off the power supply of heater. Samples 9 and 10 were re-sublimated on LEEM to observe the running droplets in real-time and -space.

3.2 *In situ* RHEED Pattern Observation

The *in situ* surface analysis of MBE experiments are obtained from RHEED which schematic representation is shown in Figure 3.4. A 15-18 keV focused electron beam is directed towards the sample at grazing angle for about 1°. The electron energy only allows the beam to penetrate through the first few atomic layers as same as 2 dimensional (2D) gratings, resulting the diffraction pattern. In the opposite position, a fluorescent screen displays the diffraction pattern. The displayed pattern on fluorescent screen is a reciprocal space representation of the sample surface.

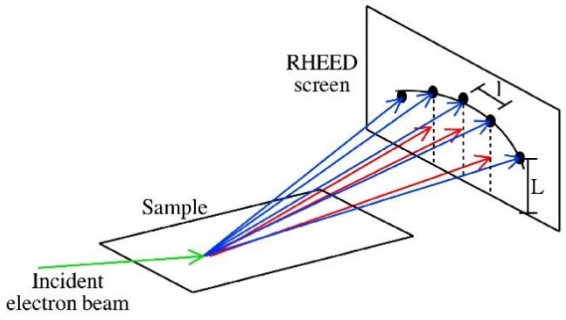

Figure 3.4 Schematic representation of a RHEED adopted from Barron, 2011 [54].

RHEED can distinguish two surface conditions: the flat and three dimensional surfaces which are indicated by the streaky, and spotty or chevron patterns,

respectively. Although the disadvantages of RHEED is not implying the size and density of three dimension structures [55].

3.3 Low-Energy Electron Microscopy (LEEM)

A low-energy/ photo-emission electron microscope (LEEM/ PEEM) is a single real-time and -space imaging system that utilizes two difference energy sources to characterize samples.

The schematic diagram of a low-energy/ photo-emission electron microscope (LEEM/ PEEM) is shown in Figure 3.5(b). In LEEM mode, A typically 20 keV collimated electron beam from electron gun is focused by illumination optics. The beam is then 60° deflected using a prism optic beam separator and directed to sample surface in UHV chamber. After that, the reflected electron beam re-enters beam separator, 60° re-deflected, and directed to imaging parts which consist of an imaging optics, an energy analyzer, a projection lens system, and a camera. In PEEM mode, the light source is just changed to UV or X-ray light source which can be produced from synchrotron radiation source. This light beam is directed towards the sample which excite, afterwards the emission from sample is deflected by beam separator to the imaging energy analyzer. The imaging analyzer also provides important data such as chemical bonding state and valence energy levels of the sample surface.

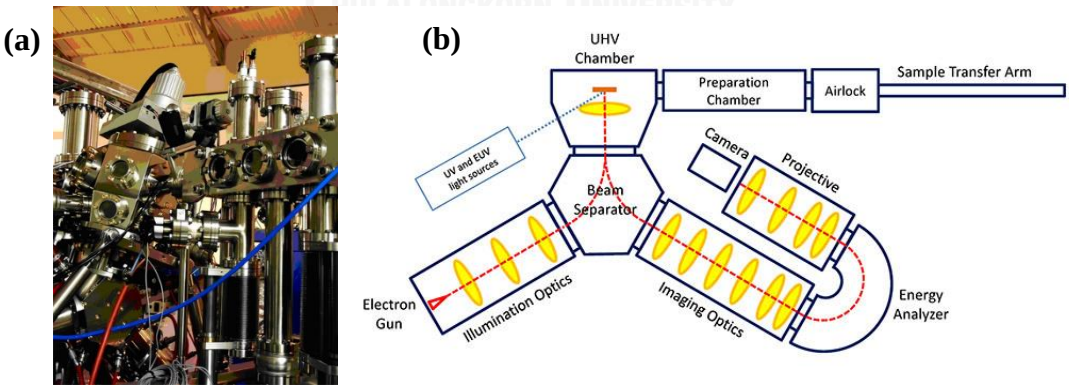

Figure 3.5 (a) Elmitec's low-energy/ photo-emission electron microscope (LEEM/ PEEM) III system adopted from synchrotron light research institute (SLRI), Thailand [56] (b) Schematic diagram of a LEEM/ PEEM adopted from okinawa institute of science and technology [57].

LEEM images sample with backscattered electrons that can give parameters for many contrast mechanism such as mirror electron microscopy (MEM), phase contrast, and diffraction contrast modes. In MEM mode, the image contrast is obtained through the electric field difference at sample surface [58]. When the sample's voltage smaller than the electron source voltage, the electron beam is fully reflected in the field above the sample surface before the beam can reach the surface region. The beam moves slowly which is easily influenced by the temporal and spatial variations of electric field.

PEEM uses photo-emitted electrons method that also provides important information about the local surface environment of the sample. For example, in UV photoemission electron microscopy (UVPEEM) mode, we can get the information about spatial maps of work function of sample surface. This information could be used to distinguish material composition.

The detailed samples preparation and sublimation in LEEM are as follows. The pre-MBE grown samples of that in Section 3.1.5 are scribed into a 1 cm x 1 cm shape and mounted onto the sample holder. The sample is loaded and pumped down in the airlock chamber. After that, the sample is transferred to the preparation chamber and baked at around 300 °C overnight to remove H_2O while the base pressure and a maximum pressure are kept below 2 x 10^{-10} Torr and 7 x 10^{-9} Torr, respectively. On the next day, the sample is introduced to the UHV chamber. Subsequently the surface is imaged with LEEM in the MEM mode and the surface oxide layer is removed by slowly ramping the sample to 580 °C by slowly increasing the filament current I_f. The sample temperature is measured by a calibrated thermocouple and pyrometer. After a 10-min oxide removal, the temperature is slowly ramped while the surface is imaged and video recorded in real time. The system base pressure is kept below 5 x 10^{-9} Torr throughout the sublimation. After sublimation, I_f is gradually decreased to zero; the sample is then removed from the UHV chamber.

3.4 Microscopy

There are three well-known microscopy techniques such as an optical, a scanning probe, and an electron beam microscopy. Figure 3.6 shows the measuring resolution comparison among several microscopy techniques e.g., optical: an optical

interference microscopy (OIM), a scanning confocal microscopy (SCM); scanning probe: an atomic force microscopy (AFM), a scanning tunneling microscopy (STM), a scanning stylus microscopy (SSM); and electron beam: a scanning electron microscopy (SEM).

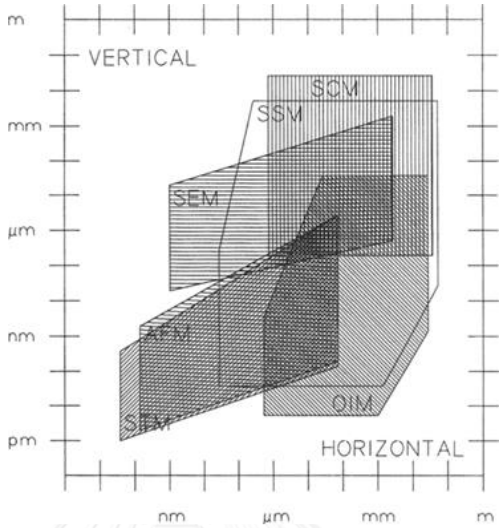

Figure 3.6 The comparison among several microscopy techniques [59].

The *ex situ* analyses of running droplet samples use three microscopy techniques such as an OIM, an AFM, and a SEM that are explained in this Section. Each of these techniques has merits and demerits. In terms of scan speed, an OIM and a SEM are faster scan speed and larger scan area than an AFM. A SEM is also equipped with the X-rays energy dispersive spectroscopy (EDS) for the chemical analysis tool. Although in terms of vertical and horizontal resolution, an AFM can provides the best details.

3.4.1 Differential Interference Contrast (DIC) Microscopy

Georges Nomarski has introduced DIC microscope about 1950s. The basic principle of a DIC microscopy makes use of interference between two light beams to form an image as illustrated in Figure 3.7. At first, a light source (1) generates a light beam, which is transformed into plane-polarized light by a polarizer (2). After that, a half-mirror (3) reflects the polarized beam into a bi-refringent prism (4). A bi-refringent prism separates the polarized beam into two partial beams directed towards the sample surface (6). These two beams are reflected by the sample towards a wave

plate (7a) and an analyzer (7); if the sample surface is flat, these beams will travel in the same time, but if there is a small step (Δh), one of these beams has to travel 2*Δh longer. Finally, this information is then processed to form image.

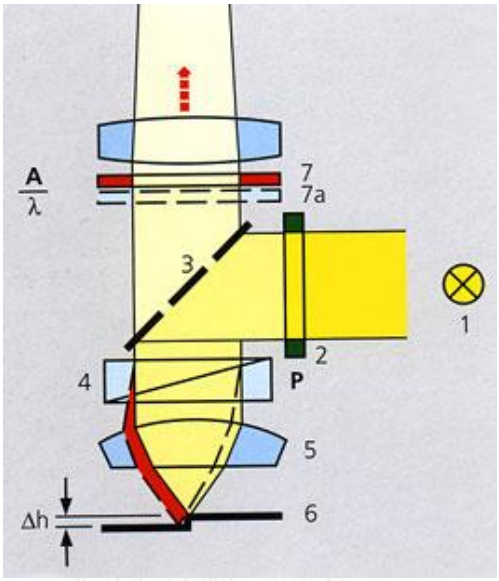

Figure 3.7 Cross-sectional schematic diagram of a DIC microscope [60].

3.4.2 Atomic Force Microscope (AFM)

In 1986, G. Binnig et al. [61] invented the rough ideas of AFM from modification of STM using the ultra small tip at the end of a cantilever as a sensitive sensor reaching the regime of interatomic force between atoms. Martin et al. [62] enhances the sensor system with vibrating cantilever and laser beam.

The working principle of AFM is shown in Figure 3.8(b). The sample is placed in a moving piezo-actuator while the cantilever tip is scanning the surface. The tip movement on the rough surface creates the change of reflection angle. The change of reflection angle is measured by a laser beam and a photo detector. The reflection angle information at each point is sent to a computer to construct the final image.

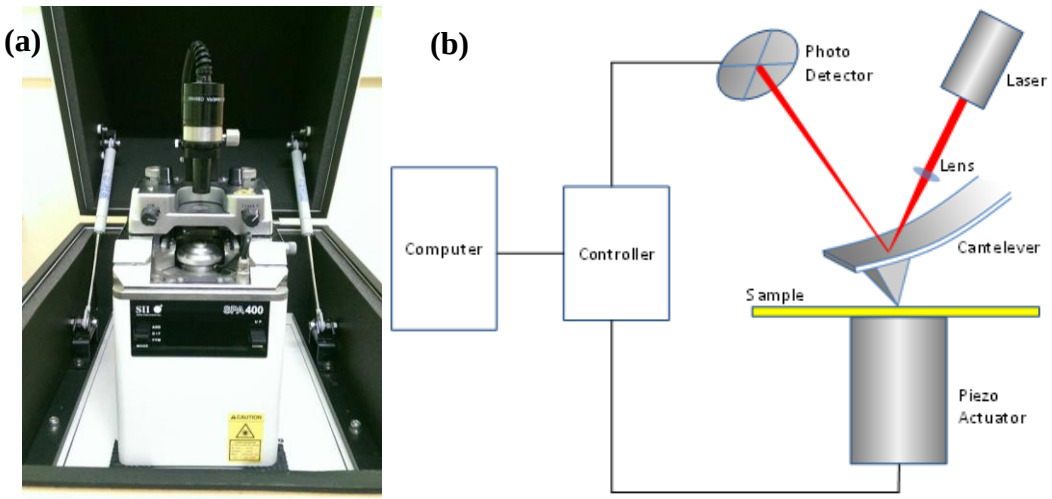

Figure 3.8 (a) A Seiko's SPA 400 AFM (b) The basic principle of AFM [63].

There are three imaging modes in AFM: contact, tapping, and non-contact modes. In the contact mode, the used force is repulsive as the cantilever tip is continuously touching the surface; the advantages are fast scan speed and good for rough surface. However during scanning, there is a possibility of the tip to damage the soft sample. In the tapping mode, the used force comes from the resonance frequency as the cantilever is not continuously touching the surface. The cantilever tip is swinging and touching the surface. An advantage of this mode is the capability to create high resolution images from easily damaged sample. In the non-contact mode, the cantilever tip is not touching the sample surface; the tip is just oscillating above the adsorbed fluid layer. The merit of this mode is very low force that has given to the surface. Hence it can extend the tip lifetime and avoid the damage to the surface.

The grown running Ga droplets samples were measured using a Seiko's SPA 400 AFM as shown in Figure 3.8(a). The AFM operates in the tapping mode. The scan parameters are as follows: scan speed is 0.5 Hz, I_{gain} is 0.4, P_{gain} is 0.2, A_{gain} is 2, and S_{gain} is 2 for the optimum of image results. The AFM image analyses are conducted using ImageJ [64] and WSXM [65].

3.4.3 Scanning Electron Microscope and X-rays Energy Dispersive Spectroscopy (SEM and EDS)

The basic principle of a SEM is to hit the small surface area with a collimated electron beam and to form an image using the reflected electron (secondary electron) beam [66] as illustrated in Figure 3.9.

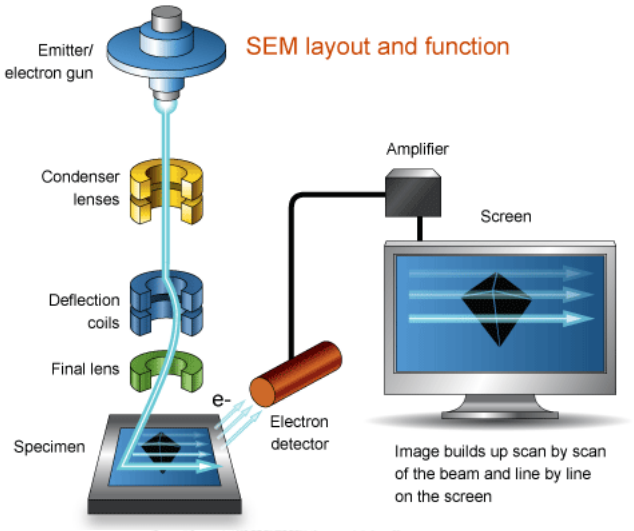

Figure 3.9 SEM layout and function [67].

In a vacuum chamber, an electron gun produces an electron beam at the top of microscope, afterwards the beam travel through a vertical path towards the sample. Before hitting the sample, the beam alignment uses set of electromagnetic lenses and coils: condenser lenses, deflection coils, final lenses control the spot size, the scanning (direction), and focus of the beam, respectively. After the beam hits the sample, some electrons are scattered, absorbed and transmitted. A detector collects secondary electrons and X-rays which are emitted from the sample. The secondary electron information at each point is sent to a computer for constructing the final image. While the X-rays emission spectrum is processed for the elemental analysis of sample surface or so-called energy dispersive spectroscopy (EDS) [68].

We used a JEOL's JSM-5410LV SEM for imaging the samples. We bombarded the sample with electron beam at accelerating voltage of 15 kV. The sample is imaged several times in low and high magnifications typically from 1000 to

10,000 times. After sample imaging, the elemental analysis is conducted using EDS system attached to the SEM.

3.5 Selective Ga Droplets Etching

The selective Ga droplets etching uses commercial 37 % hydrochloric acid (HCl) together with deionized water for dilution. The detailed chemical mixing is presented in Appendix.

Sample 7 is subject to selective Ga droplets etching using two different chemical concentrations; this sample is scribed into a 0.5 cm x 0.5 cm so that the surface condition before and after etching can be easily compared. The chemical etching recipes are as follows. At first, the scribed sample was dipped in a HCl:H_2O (1:5) solution which is adopted from Elborg, et al [69]—without stirring—for 30 min. With this etching, the Ga droplets are not completely etched away so the scribed sample is re-etched with the second recipe: the scribed sample was dipped in a HCl:H_2O (1:2) solution—with stirring—for 15 min. After etching, the sample was rinsed in deionized water. Subsequently, the surfaces before and after etching are compared using a DIC microscopy.

3.6 Sharp Tungsten (W) Tip Fabrication and Droplet *I-V* Characterization

The droplet fabrication is conducted under UHV, ensuring the cleanliness and the purity of MS junction. So the *I-V* and *C-V* measurements will show the results that closer to *"the true value"*. By this measurement set-up, Equation (2.10) and (2.11) from Section 2.6 can be examined and proven.

The electrical measurements on small areas using sharp tip has been conducted since 1950s. Shockley et al. [70] measured the *I-V* characteristic of a type A transistor using this technique. In droplet electrical characterization, we used a sharp W tip for microcontact, touching the Ga droplet.

The fabrication of W tip as exemplified by Figure 3.10(a) uses electrochemical etching mechanism. The experimental set-up is as follows. The anode (working electrode) is a W wire and the cathode (counter electrode) is a piece of copper (Cu); they are placed apart to avoid the H_2 gas bubbles from cathode disturbing the W etching. A 2 M KOH solution serves as the electrolyte—the detailed solution

preparation is given in Appendix. The W wire is need to be placed in the perpendicular direction to the electrolyte using a static holder to avoid the irregular shape of tip after etching. The W wire is about 6 cm in length, 0.05 cm in diameter, and it immersed at about 0.5 cm below the KOH surface. The W wire and the counter electrode are connected to an Advantest TR6143 DC voltage current source/ monitor that is used to generate the bias voltage and to monitor the current that pass through the electrodes. The electronic control is manual using the ON/ OFF button on the DC voltage source.

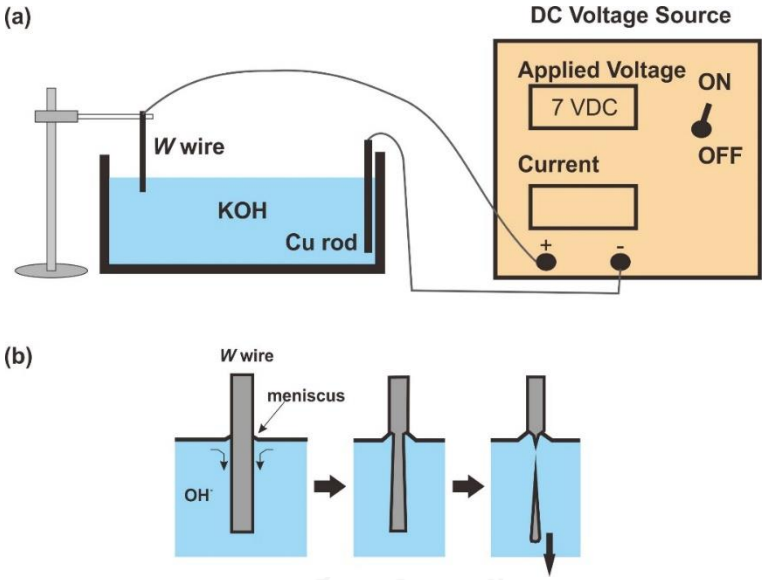

Figure 3.10 The schematic diagrams showing (a) the experimental tip-electrochemical etching station and (b) the dynamic of electrochemical etching.

The detailed chemical reactions and experimental procedure of the W wire electrochemical etching are as follows. The chemical reaction of KOH and water mixing is

$$KOH_{(s)} + H_2O_{(l)} \rightarrow K^+_{(aq)} + OH^-_{(aq)} + H_2O_{(l)} \quad (3.1)$$

After reaching equilibrium, the mixing of KOH and water results the solvated ions: the K^+ ions and the OH^- ions which conduct electricity troughout the solution.

Afterwards, when the electrochemical etching station is ready, the voltage source is turned-on and the static bias voltage is adjusted—in our case, we use 7 VDC.

Immediately after the bias voltage is applied to the electrodes, the electrochemical etching reaction starts.

During etching, only the OH^- ions take part in the reactions while the K^+ ions just "look on"—sometimes referred to as spectator ions [71]—because the OH^- ion has an oxidation potential of 0.401 V [72] which is higher (more positive) than that of the K^+ ion: about -2.931 V [73]. The oxidation potential measures the tendency of a chemical to acquire electrons, so that the chemical species with a higher oxidation potential is likely to take part in an electron-transfer reactions e.g., oxidation-reduction: the electrochemical etching reactions. Hence, the underlying chemical reactions of electrochemical W etching are [74]

$$\text{cathode: } 6H_2O_{(l)} + 6e^- \rightarrow 3H_{2(g)} + 6OH^-_{(aq)} \quad (3.2)$$

$$\text{anode: } W_{(s)} + 8OH^-_{(aq)} \rightarrow WO_4^{2-}{}_{(aq)} + 4H_2O_{(l)} + 6e^- \quad (3.3)$$

$$W_{(s)} + 2OH^-_{(aq)} + 2H_2O_{(l)} \rightarrow WO_4^{2-}{}_{(aq)} + 3H_{2(g)} \quad (3.4)$$

The current decreases linearly with time during etching because the resistance of the W wire increases when the area of the W wire in the electrolyte decreases. At a certain cut-off time—about 10 min in our case—the W wire eventually breaks at a neck region near the KOH surface of which the etching is formed as illustrated in Figure 3.10(b). Afterwards, the current rapidly drops and the voltage is quickly switched off. After etching, the W wire was thoroughly rinsed in deionized water. Without further cleansing, the W wire is ready for droplet *I-V* characterization.

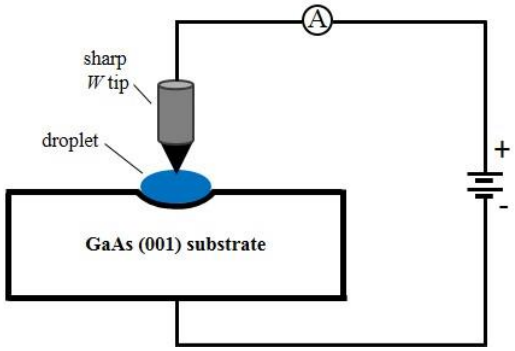

Figure 3.11 The schematic diagram showing droplet *I-V* characterization using sharp W tip as microcontact touching droplet surface.

The detailed set-up of the droplet *I-V* characterization is shown in Figure 3.11. The sharp W tip is touching the metallic Ga droplet and the backside contact is using an aluminum foil. The Cu wire connects the W tip, the voltage source/ pA meter, and the backside contact, forming the closed-circuit connection. A HP 4140 B DC voltage source applies bias voltage at a selective range and step: (-0.7 to 0.7) V and 0.01 V, while it is also taking current measurements at each bias voltage points. Afterwards, a computer equipped with NI LabVIEW software collects and process these data. We perform the *I-V* measurement twice: under optical microscope (OM) light illumination and in the dark (dark *I-V*).

CHAPTER 4
Results and Discussion

This chapter reports the key results of the experiments which are divided into five Sections. Section 4.1 presents reliable synthesis of self-running Ga droplets on GaAs (001), providing the alternative growth design in MBE. Section 4.2 and 4.3 explain the chemical constituent analysis and selective Ga droplets etching, respectively. Section 4.4 presents the W tip fabrication and the preliminary results of droplet *I-V* characterization, giving basic understanding of metal-semiconductor (MS) junction. Finally, Section 4.5 explains the manipulation of self-running Ga droplets migration.

4.1 Reliable Synthesis of Self-Running Ga Droplets in MBE

The first step of producing self-running Ga droplets in MBE is the reference condition establishment. Samples 1 and 2 establish the reference condition where all samples undergo the surface condition of these samples. Sample 1 shows the thermal oxides desorption stage, whereas sample 2 shows the chevron patterns—the critical stage patterns.

The second step, we register the temperature when the chevron patterns appear and use this temperature as referenced temperature T_0 to make reliable formation of running Ga droplets. We sublimate samples 3 to 6 according to T_0 and temperature profiles as described in Figure 3.2. Running Ga droplets are reliably produced in all these samples.

4.1.1 Thermal Oxide Desorption

In general, the oxides desorption of GaAs occurs twice: desorption of (1) very volatile As-oxides and (2) Ga-oxides. As-oxides evaporate at a lower temperature than Ga-oxides. For sample temperature ~ 300 ºC, the As-oxides desorption occur and the underlying reaction is [75, 76]

$$As_2O_3 + 2\ GaAs \rightarrow Ga_2O_3 + 2\ As_2 \text{ or } As_4\uparrow \qquad (4.1)$$

When the sample temperature further increases to ~ 500 ºC, the Ga-oxides desorption takes place and the another reaction appears [75, 76]

$$Ga_2O_3 + 4\ Ga \rightarrow 3\ Ga_2O\uparrow \qquad (4.2)$$

Theoretical temperature of thermal oxides desorption is ~ 580 ºC [77, 78], although the thermocouple temperature reading of 6 samples varies between 550 °C and 591 °C under this condition due to the thermocouple uncertainty. For sample 1, thermal oxides desorption is observed at 591 °C, which is directly known from the broadening of RHEED spots into the streaky patterns as shown in Figures 4.1(a) and 4.1(b). The streaky patterns indicate the mass transport of Ga-oxides according to reaction (4.2) which also create the surface corrugation as seen from the *ex situ* AFM image in Figure 4.1(c). In this stage, the root mean square (RMS) roughness is about 5.67 nm.

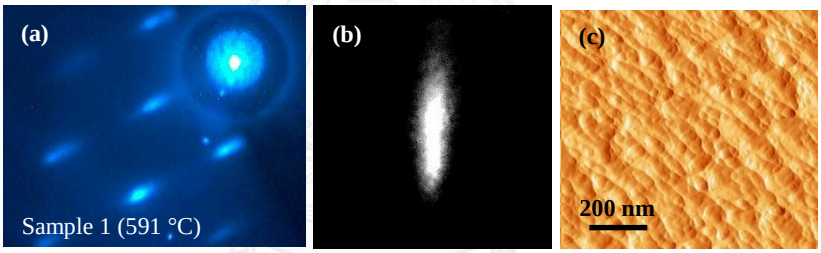

Figure 4.1 (a) The streaky patterns taken from the [1-10] azimuth and (b) the extracted pattern from the (00) diffraction index during thermal oxides dexorption. (c) The AFM image reveals surface corrugation at this stage.

4.1.2 Chevron Patterns

After 30 min of thermal oxides desorption, the sample temperature increases while the RHEED patterns get shorter as shown in Figure 4.2(d). Until the patterns completely change into the chevron patterns at a certain thermocouple temperature, hereinafter referred to as T_0, which varies between 611 °C and 640 °C for 5 samples.

Figures 4.2(a) and 4.2(b) show when the chevron patterns appear in sample 2, at T_0 = 611 °C. The shape of these patterns are similar to those of QDs growth patterns [55], indicating the initial stage of 3D structure formation. AFM image in

Figure 4.2(b) reveals that these patterns correspond to the surface grains formation with RMS roughness of about 8.96 nm.

The difference between the observed chevron patterns in QDs growth and Langmuir evaporation is as follows. For QDs growth, the chevron patterns indicate the strain relaxation of the lattice-mismatched crystals. Whilst for Langmuir evaporation, the patterns show the initial stage of nanoscale droplets formation. On the Ga-rich surface, Ga adatoms are very mobile [79] and they merge to form the droplets.

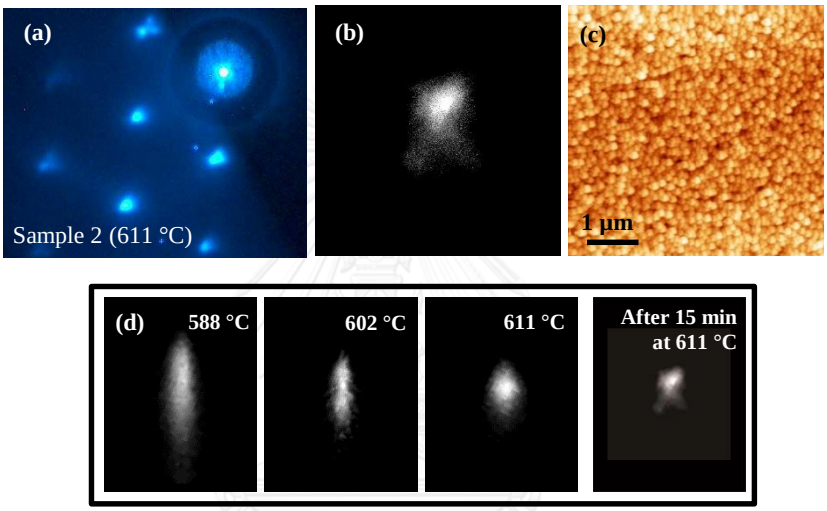

Figure 4.2 (a) The chevron patterns taken from the [1-10] azimuth and (b) the extracted pattern from the (00) diffraction index. (c) AFM image shows nanoscale droplets formation at this stage. (d) RHEED patterns evolution during sublimation of sample 2 extracted from the (00) diffraction index.

The further increase of sample temperature results in the RHEED pattern's decay and disappearance. The origin of RHEED pattern disappearance is expected from the nucleation of liquid phase Ga droplets which make the diffused RHEED beam as seen previously in the droplet-epitaxial QDs growth [80]. In addition, the typical diameter and height of running Ga droplet are about 1.9 µm [5] and 1.4 µm [6], respectively, then the droplet may blocks, absorbs, or scatters the electron beam from RHEED so that the beam is not properly hitting the fluorescent screen.

4.1.3 Running Ga Droplets

Although RHEED do not provide surface information during sublimation, running Ga droplets can still be produced using the sublimation according to T_0. Samples 3 to 6 use T_0 as reference for sublimation where the temperature profiles are shown in Figure 3.2.

Sample 3 is sublimated at the highest temperature of T_0 +20 °C but for the shortest duration of 30 min. After quenching the sample, DIC images are taken showing the non-uniform surface morphology as indicated in Figure 4.3. Figure 4.3(a) shows the distribution of small running Ga droplets while Figure 4.3(c) shows the majority of immobile big droplets. These indicate the different stages of non-congruent evaporation on the surfaces: the small droplets correspond to earlier stage than the big droplets, caused by temperature non-uniformity [81].

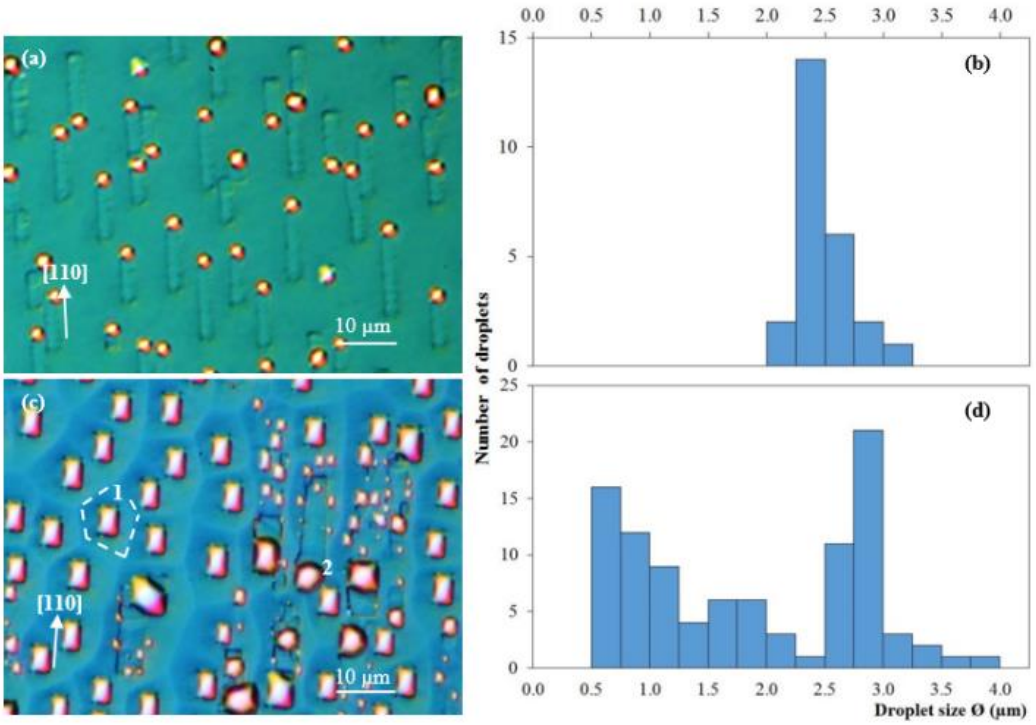

Figure 4.3 (a) The DIC image of sample 3 showing running Ga droplets on GaAs in the cold zone areas with (b) the corresponding size histogram of droplets differ remarkably from (c) the DIC image in the hot zone areas with (d) the corresponding size histogram of droplets.

The non-uniformity is reasonable since sample 3 is not well-prepared as the unevenness of In glue backside creates non-uniform thermal contact. By viewing the front surface and againts the backside of sample, it is clearly visible that the gray surface areas are occupied by large light-scattering droplets while the aligned backside is having much In glue. Good thermal contact is obtained in these areas, hereafter referred to as “hot zones”. The shiny surface areas are occupied by small droplets while the aligned backside is almost In glue-free. Poor thermal contact is obtained in these areas, hereafter referred to as “cold zones”.

The surface morphologies of the cold zones and the hot zones were obviously different. Figures 4.3(a) and 4.3(b) show the DIC images of the cold zones and the corresponding size histogram of droplets, respectively. Apparently the droplets have been running during sublimation as the running trails are visible. The running trails reveal that the droplets run along [110] or [-1-10] directions with approximately equal probabilities, in good agreements with previous studies [4, 13]. The running droplets in the cold zones are the first generation or primary droplets, with diameter ranging from 2 μm to 3.5 μm, supporting the 1.9-μm critical size previously reported by Wu et al [5].

Figures 4.3(c) and 4.3(d) show the DIC image of the hot zones and the corresponding size histogram of droplets, respectively. It can be seen the existence of two types of droplets: the primary droplets having a diameter in the range of about 2.4 to 4 μm and the secondary droplets having a diameter as small as 0.5 μm. The surface indicates the late stage coalescence growth [82] which has been reported on various III-V surfaces e.g., InP [83] and GaAs [14] before the first reported self-running phenomenon [4]. The running trails are not formed, possibly because the simultaneous formation of droplets on the surface results in high density droplets and the scarcity of space for the running droplets. The simultaneous formation of droplets is caused by the rapid decomposition: the sample is sublimated either at a temperature that too high or too fast ramping rate [25]. A droplet grows and reaches critical size which depending on the surrounding of its occurrence, may be mobile or immobile. Figure 4.3(c) shows the mobile (marked 1) and immobile (marked 2) droplets. The immobile droplet is surrounded by the boundaries (denoted as dashed lines),

restricting its motion. In contrast, the droplets in the cold zones and the mobile droplet in Figure 4.3(c) are free from the boundaries; they move around with ease.

The typical shape of the mobile and the immobile droplets are different: circular for the mobile and rectangular for the immobile droplets. The origin of rectangular shape is from the confining of contact line along ±[110] and ±[1–10] on GaAs (001) surface during the sticking state [22]. In the slipping state, contact line less confined by the {111} planes, the droplets get more circular, suggesting the same behaviour with liquid droplet in surface grooves [84, 85]. The droplet shape cycles between circular and rectangular during stick-slip motion as reported by Shorlin et al. [14].

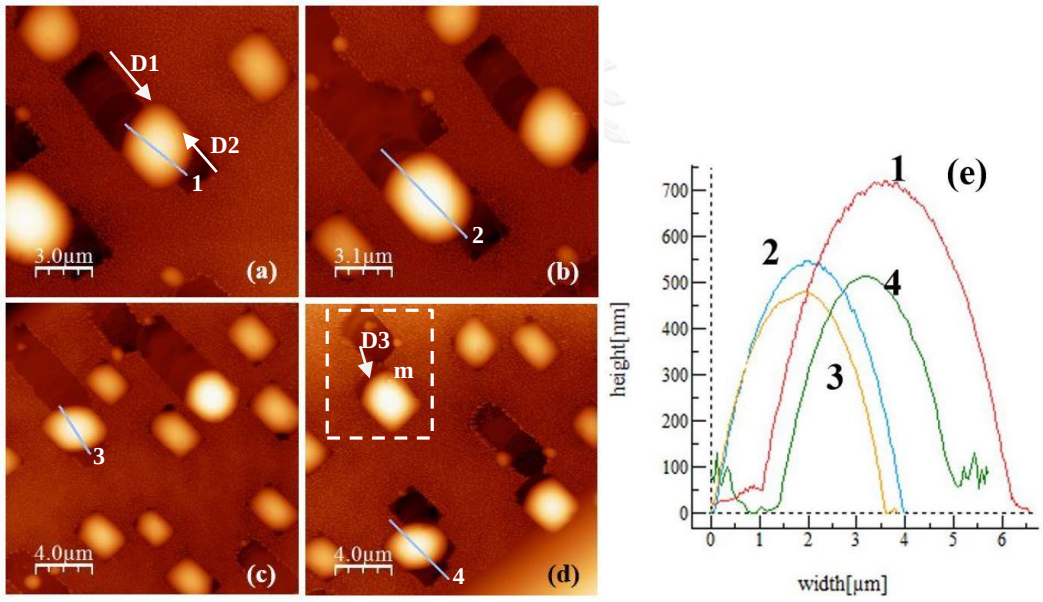

Figure 4.4 (a, b, c, and d) the AFM images of sample 3 showing post-coalescence events between two running droplets with (e) the correspoding AFM line-scanning profiles.

In the areas between the hot and cold zones of sample 3, hereafter referred to as "intermediate zones", we observe coalescence of running droplets as shown in Figure 4.4. The existence of two running trails nearby big droplets (shown as 1, 2, 3, and 4) indicates two droplets that have undergone coalescence and merged into one big droplet. For example, droplet 1 Figure 4.4(a) is the result of coalescence of two droplets that previously occupied the adjacent running trails (marked with arrows D1

and D2). These two droplets move toward each other and reactively coalesce into droplet 1. We expect the similar chronology for the formation of droplets 2, 3, and 4.

Droplets coalescence occurs in a reactive system, as clearly illustrated in Figure 4.4(d) (the dashed-lines box). Before a coalescence, a droplet occupies the etch pit, marked as D3, and a droplet occupies the position *m*. The droplet in the *m* position possibly larger than the droplet in the D3 position, so that during a coalescence, the droplet in the D3 is detached from the pit and merged to form one larger droplet in the *m* position, this is in accordance with the theory of reactive wetting in Section 2.4.3. After coalescence, the droplet size and height increase where the observed post-coalescence height of droplets varies between 475 nm and 720 nm as shown in Figure 4.4(e).

Samples 4 and 5 are sublimated at T_0 + 10 °C and T_0 + 5 °C, for 60 and 90 min, respectively. After quenching the samples, DIC images are taken; its showing the uniform formation of running droplets in the both samples because the backside In glue is uniformly distributed.

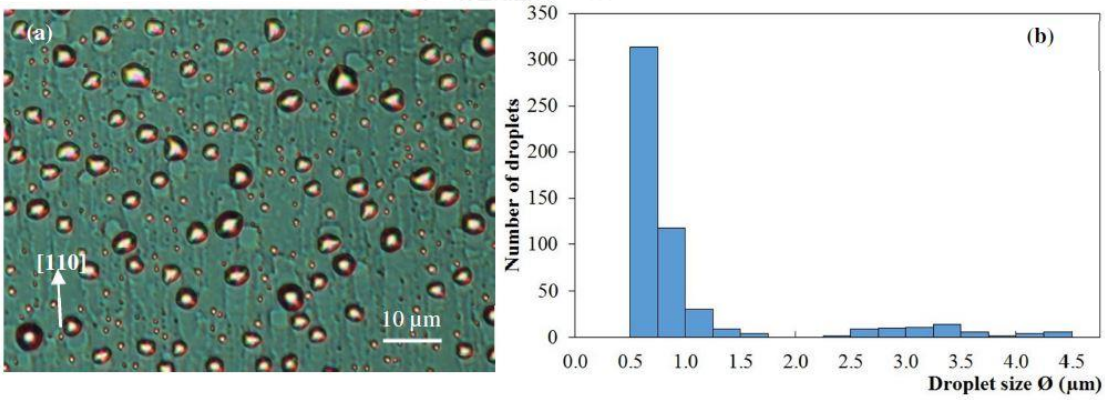

Figure 4.5 (a) the DIC image showing the surface morphology of sample 4 with (b) the corresponding size histogram of droplets.

The surface morphologies of samples 4 and 5 are relatively similar: full of small, secondary Ga droplets, as shown in Figure 4.5 and 4.6. However, the running trails also exist in both samples, indicating that the droplets have been running during sublimation. The majority of the running trails is created from the running of primary droplets where the largest diameter of these droplets is approximately 4.5 µm for sample 4 and 7.5 µm for sample 5.

The size of primary droplets in sample 5 is larger than those in sample 4. This may happen because sample 5 is subject to longer (15 min) sublimation than sample 4 despite being sublimated at a slightly lower (5 °C) temperature. The 5 °C difference is within the uncertainty of registering T_0 from sample to sample.

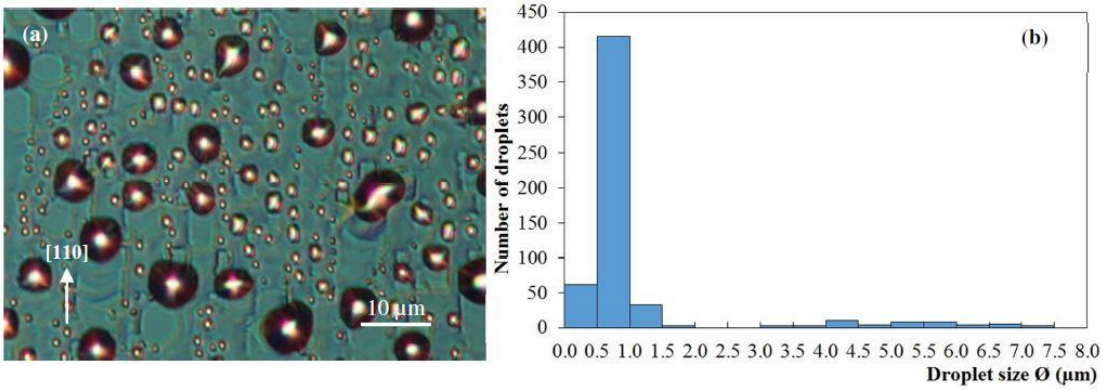

Figure 4.6 (a) the DIC image showing the surface morphology of sample 5 (b) with the corresponding size histogram of droplets.

The histograms of samples 4 and 5 show that the droplets grow according to Ostwald rippening theory [86]: larger Ga droplets grow at the expenses of smaller Ga droplets. As can be seen, the medium-sized Ga droplets (2-4 µm) of sample 5 are less than that of sample 4.

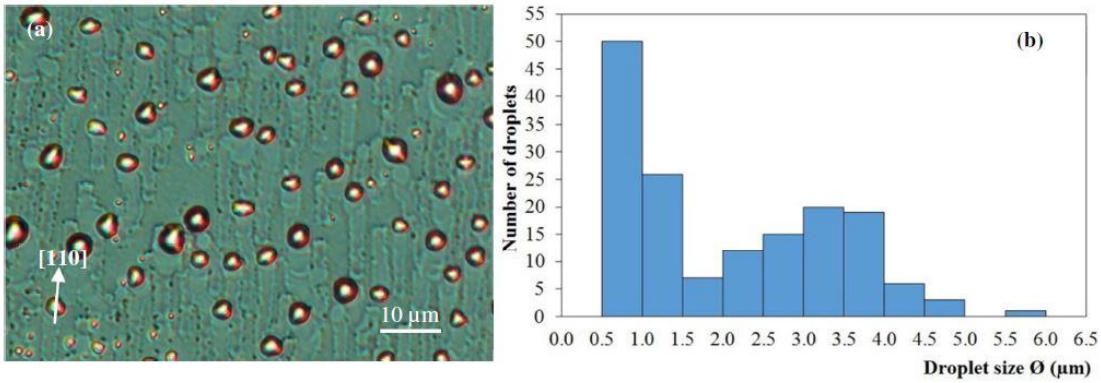

Figure 4.7 (a) the DIC image showing the surface morphology of sample 6 with (b) the corresponding size histogram of droplets.

Sample 6 is sublimated at the lowest temperature of T_0 – 30 °C but for the longest duration of 75 min. The DIC image of sample 6 after quenching is shown in Figure 4.7(a). In contrast to samples 4 and 5, the surface morphology of sample 6 is

primarily occupied by medium-sized Ga droplets (2-4 μm) with a smaller number of small, secondary droplets (< 1.5 μm). The apparent decrease in the number of secondary droplets is possibly associated with droplets shrinking as the temperature decreases to T_0 – 30 °C. We already know that droplets tend to shrink while dwelling at a temperature below T_c from Section 2.3. Thus, one might conclude that T_0 – 30 °C is lower than T_c. In addition, at a temperature of T_0 – 30 °C, the estimated average droplet velocity is 10-15 μm/hour (this velocity was obtained from dividing the distance traveled (the average of trails) by the sublimation duration).

4.2 Chemical Constituent Analysis

Besides the surface morphology, there is also important information about the chemical constituents of the post-sublimated sample, which is studied using Energy Dispersive Spectroscopy (EDS) in a SEM microscope.

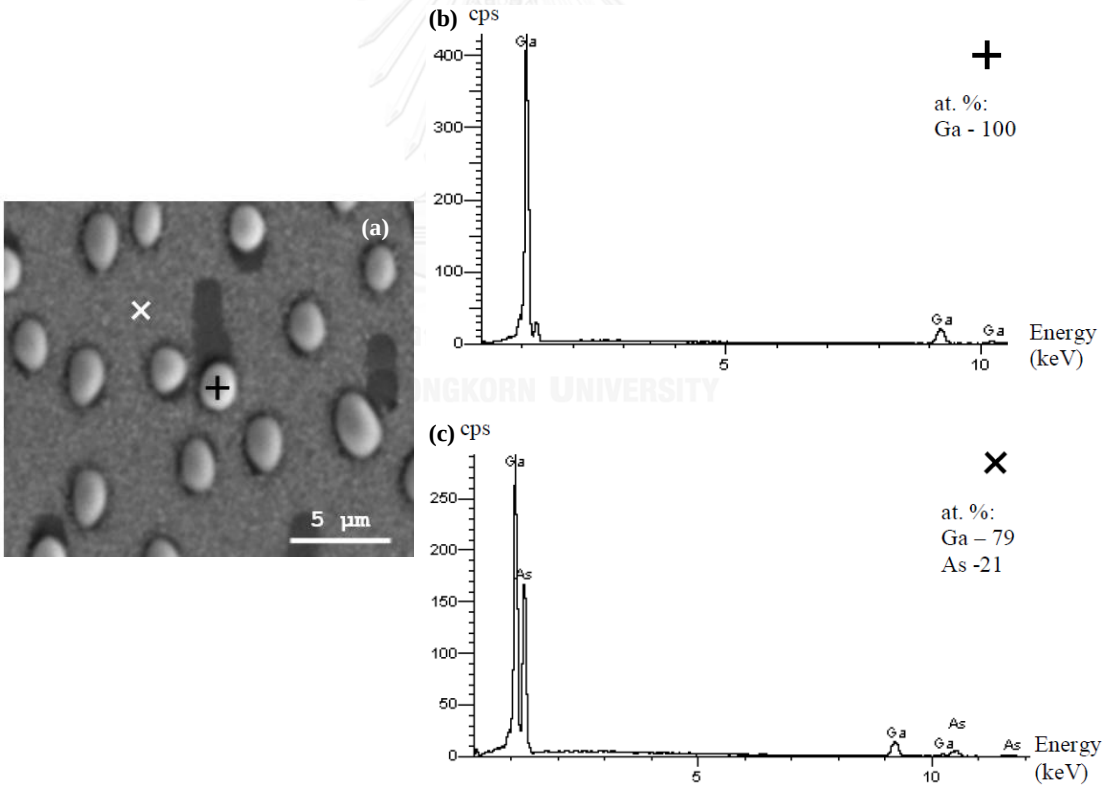

Figure 4.8 (a) the SEM image showing gallium droplets on GaAs (001); EDS point analysis locations indicated by the plus (+) and the multiplication (x) signs in the corresponding SEM image. The elemental composition results of indicated locations (b and c) are presented.

A 15 kV electron beam is bombarded to the sample at a selected locations marked with plus (+) and multiplication (x) signs as shown in Figure 4.8(a). EDS spectra extracted from these locations are shown in Figures 4.8(b) and 4.8(c). The droplet, marked with +, contains of Ga for about 100 %, indicating it is purely liquid metallic Ga. Whereas the flat surface, marked with x, contains of 21 % As and 79 % Ga, indicating the surface is not perfectly smooth as much portion of As evaporates.

4.3 Selective Ga droplets Etching

The selective etching can also examines whether the droplets are formed from liquid Ga. If the droplets are disappeared, one can sure that the droplets are Ga, otherwise they are not Ga.

Surface morphology of sample 7 before the chemical etching is shown in Figure 4.9(a). The surface is populated by large and small Ga droplets which is the characteristic of late-stage coalescene [14].

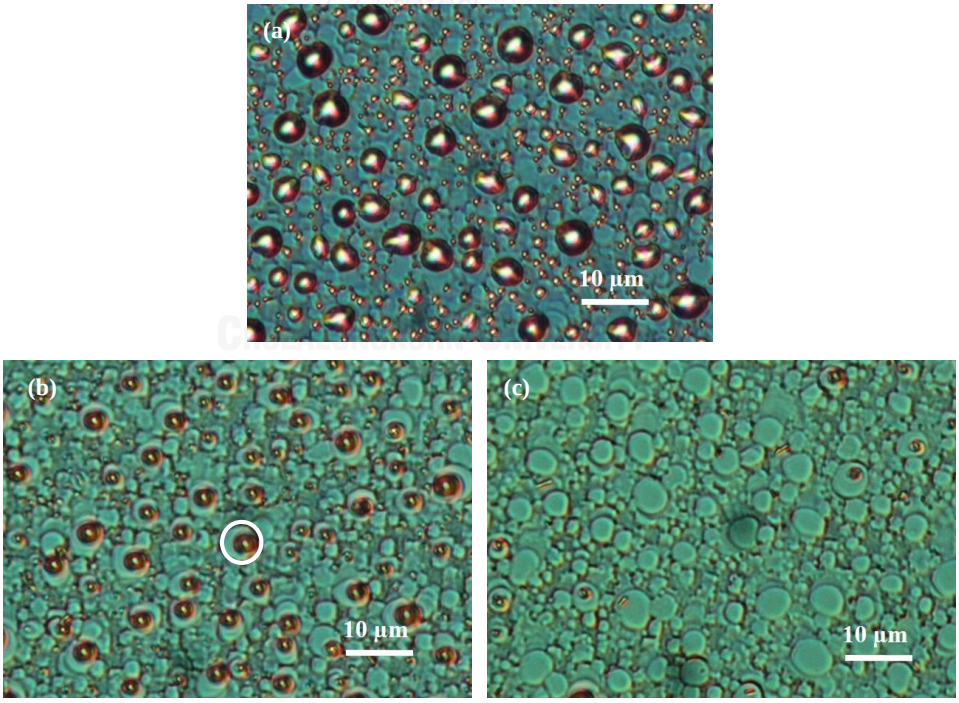

Figure 4.9 The DIC images showing surface morphology of sample 7 (a) before selective etching (b) after 30 min selective etching in a HCl:H_2O (1:5) solution—without stirring (c) after 15 min re-etched in a HCl:H_2O (1:2) solution—with stirring.

Surface morphology of sample 7 after the etching in a HCl:H_2O (1:5) is shown in Figure 4.9(b). The Ga droplets are not completely removed, however the Ga droplets have become smaller relative to the size before the etching. As illustrated by circle in Figure 4.9(b), a Ga droplet was previously fulfill the etch pit; this droplet size is reduced by half, leaving a half-fresh exposed pit. The incomplete etching of Ga droplets using this recipe may be caused by two possibilities: (1) the recipe source [69] is not mention about the initial concentration of HCl—possibly have a higher concentration—so that it is difficult to reproduce the recipe only using HCl and water ratio, or (2) the chemical reaction does not perfectly conducted because the solution is not stirred during the etching. Therefore, for the second recipe, we improve by increasing the concentration and stirring the solution.

Surface morphology of sample 7 after the etching in a HCl:H_2O (1:2) is shown in Figure 4.9(c). Almost the entire Ga droplets are removed from the surface with only negligibly amount of GaAs was etched in this solution. The second etching creates the curved etch pits which are in agreements with the droplets shape. The recipe appears to work well and may be used in further selective Ga droplets studies. With this recipe, the initial concentration of HCl and the mixing treatment are already known, so the etching can be repeated accordingly.

4.4 Droplet *I-V* Characterization

This part explains the preliminary results of droplet *I-V* characterization, which is divided into two sections. Section 4.4.1 explains the sharp W tip fabrication result and the tip-droplet alignment. Section 4.4.2 reports droplet *I-V* curves and analyses.

4.4.1 Sharp W Tip Fabrication

Figure 4.10 shows a succesfull electrochemically etched W tip with sharp curvature (diameter≈1 μm): small enough to touch the primary Ga droplets that typically have diameters of (2-4) μm.

To get a successful etched W tip, one must consider the following factors during the etching. First, after the W wire drop-off from the tip, the DC voltage source must be immediately turned off to prevent a prolonged etching. Because the etching

reaction still occurs despite the W wire drop-off, so if the voltage source is not turned off, the sharp end of the W tip will also be etched, resulting in the blunt tip as reported in many previous tip etching studies [74, 87, 88].

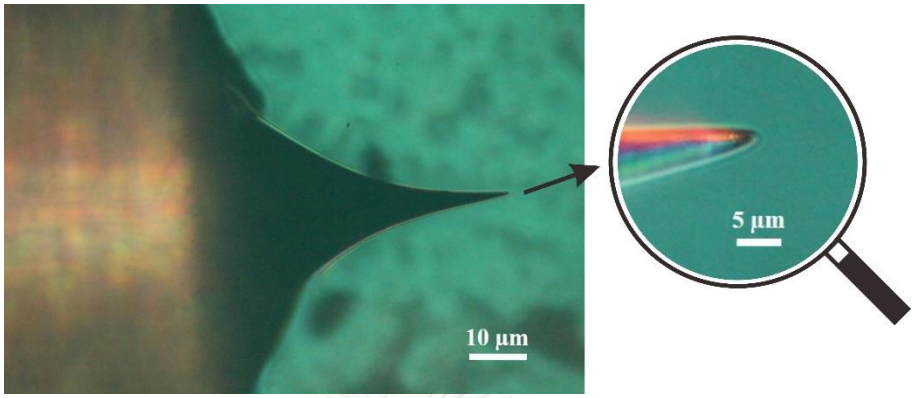

Figure 4.10 The DIC images showing sharp W tip fabricated by the electrochemical etching (left) together with the magnified scale image of curvature (right).

Second, the etching station must be placed in a vibration-free table, otherwise the irregular shape of tip as exemplified by Figure 4.11(a) will be obtained. This tip is unintentionally exposed to a vibration during the etching until the immersion depth changes and results that wavy shape.

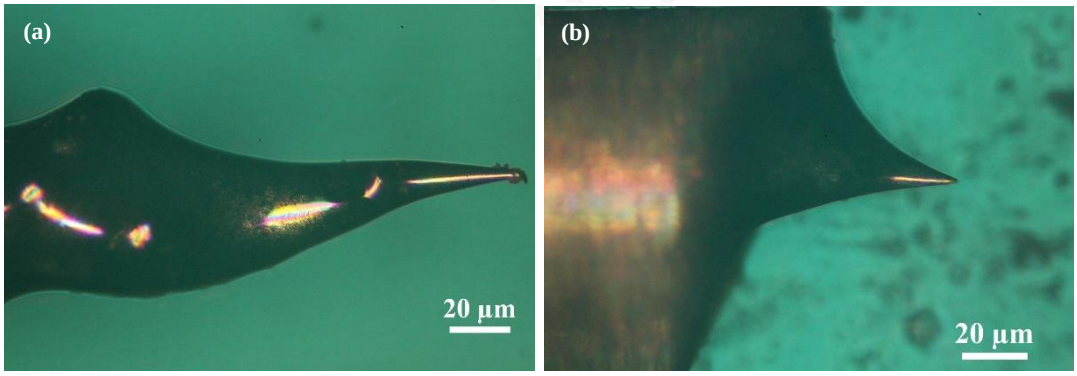

Figure 4.11 The irregular shapes of tip due to (a) the vibration and (b) the non-perpendicular contact between the W wire and the electrolyte.

Third, the W wire must be placed perpendicular to the electrolyte surface. If the W wire is not perpendicularly with the electrolyte surface, the asymmetric shape of tip will result as shown in Figure 4.11(b). However, finding a good immersion

arrangement between the W wire and the electrolyte surface is not easy. One trick is to use the short W wire (not exceeds 6 cm), so that easy to control the immersion angle. The successful etched W tip is then used for a microcontact, touching the Ga droplet. The tip is placed in a linear stage, allowing precisely controlled and targeted tip movements. The alignment of this tip and a Ga droplet is shown in Figure 4.12. The tip easily reaches the Ga droplet with diamater ≥2 μm, despite sometimes the Ga droplet—liquid at room temperature—clings to the tip. To clean the sticky Ga from the tip, we wipe the tip using acetone. Once the alignment is completed, the *I-V* measurement can be initiated.

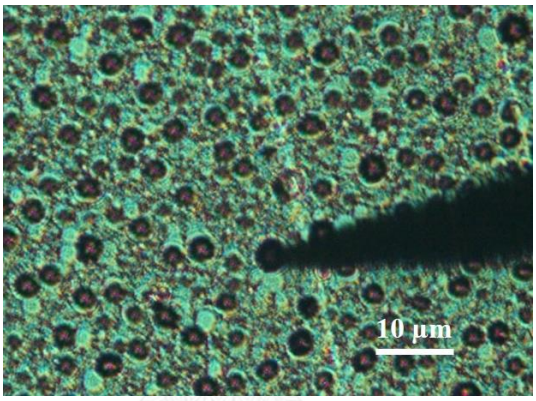

Figure 4.12 The DIC image showing the alignment of a sharp W tip and a Ga droplet in sample 8.

4.4.2 Droplet *I-V* curves

The *I-V* curves of a Ga droplet in GaAs (001) as exemplified by Figure 4.13 can be treated similar to those of a solar cell, containing important parameters such as the open circuit voltage (V_{oc}) and the short circuit current (J_{sc}). The open circuit voltage is the voltage when there is no current passing through the junction ($J=0$) and the short circuit current is the current in the 0 impedance ($V=0$).

For the dark *I-V* curve (-Δ- signs), V_{oc} and J_{sc} fall about 0 but for the under optical microscope (OM) light *I-V* curve (-o- signs), they fall at non-zero values: V_{oc} is 0.07 V and J_{sc} is -7.616 mA/cm^2. The illumination of OM light creates the shifting of *I-V* curve into the fourth-quadrant—the working region of a solar cell. Assuming this droplet-semiconductor junction is a solar cell, under OM light illumination it

generates the maximum power P_{max} of about 0.146 mW/cm^2 at the maximum power point (0.03 V, -4.866 mA/cm^2) as marked with arrow in Figure 4.13.

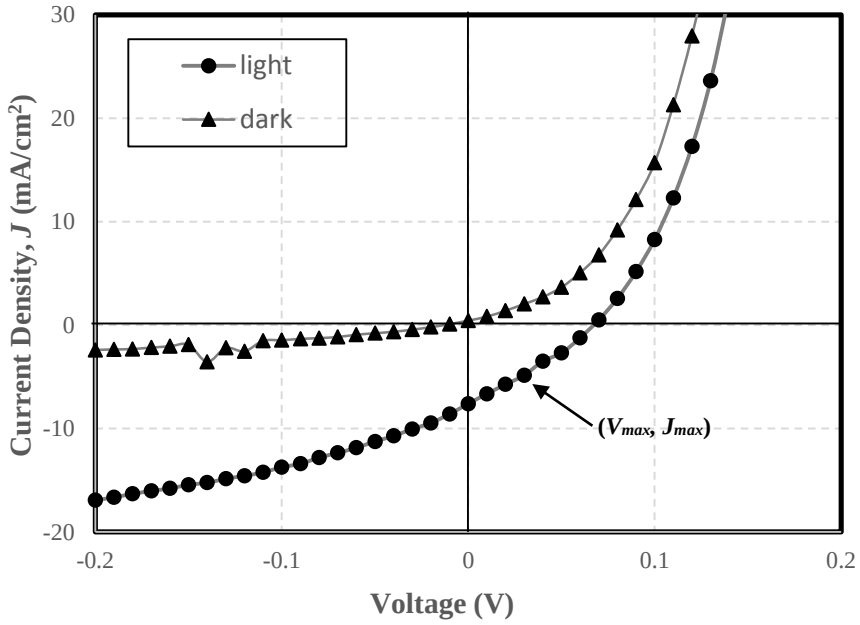

Figure 4.13 The dark and under optical microscope (OM) light *I-V* curves from the measurement of a Ga droplet on GaAs (001) in sample 8 with linear scale.

The *I-V* curve with linear scale can not provide the important MS junction parameters, e.g., the reverse saturation current and the ideality factor. To extract these parameters, the plot of $\log_{10}(I)$ vs V (the semi-logarithmic plot) is used; it also effectively expand the scale for small currents.

Figure 4.14(a) shows the semi-logarithmic plot of dark *I-V* curve of Figure 4.13. The negative current on the third-quadrant can not plotted as log-scale, therefore it values are normalized and transferred to the second-quadrant.

In the first-quadrant, the semi-logarithmic plot can be separated into three different regions: region 1, region 2, and region 3. Region 1—where the leakage currents and the depletion region recombination are dominant—is the non-linear region at low forward bias voltages. Region 2—where the band-to-band recombination is dominant—is the ideal diode region and the semi-log plot

characteristic is linear. Region 3 is the non-linear region due to the current limitation by the series resistance [89].

The device characteristic is determined through trend-line estimation in region 2 from dark *I-V* curve. Figure 4.14(a) shows the trend-line (red line) of dark *I-V* curve in the first-quadrant.

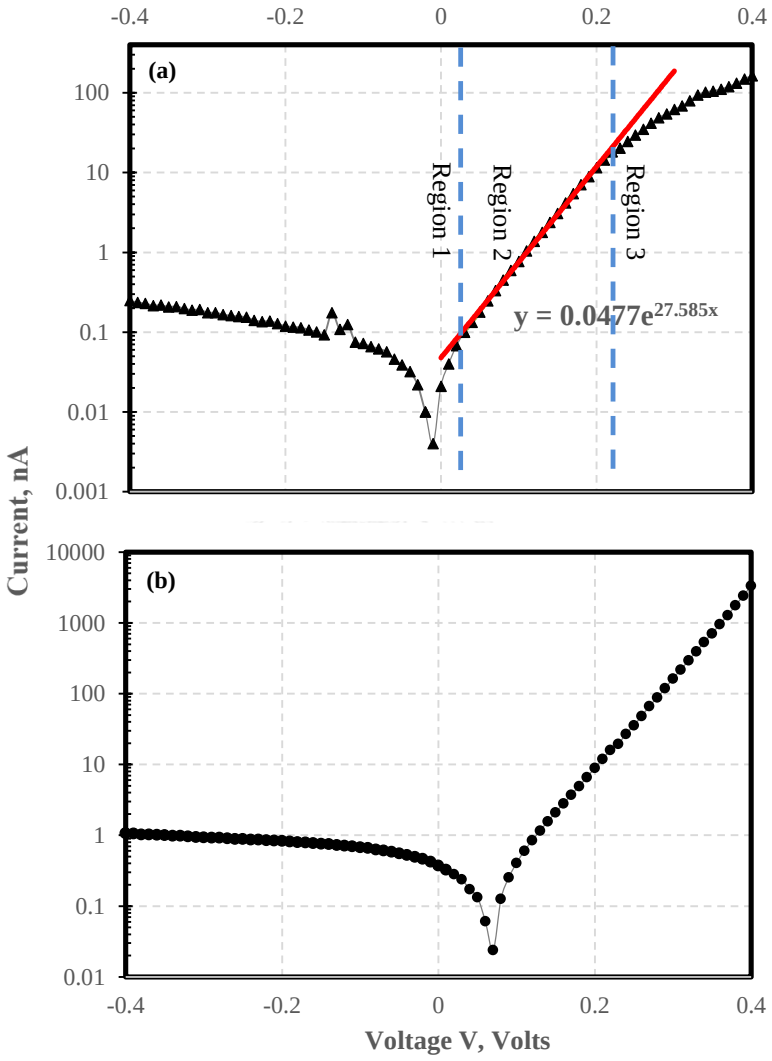

Figure 4.14 The semi-logarithmic plots of (a) dark and (b) under OM light *I-V* curves of Figure 4.13.

From Excel we found that the equation approximation that fit to the data is $I=Aexp^{\alpha V}$, where A=0.0477 nA and α=27.585. While from the mathematical model in

(2.19), when $V > 50\text{-}100\ mV$ the -1 term is negligibly small, so the equation can be reduced into

$$I = I_{sat}\left[\exp\left(\frac{qV_b}{nkT}\right)\right] \tag{4.1}$$

Equation (4.1) is in conformity with the Excel approximation and thus we must obtain

$$I_{sat} \approx A = 0.0477 \text{ nA} \tag{4.2}$$

$$\frac{qV_b}{nkT} = 27.585 \tag{4.3}$$

Our measurement is conducted in room temperature, where *kT/q*—the thermal voltage— is approximately 25.85 mV [90]. Thus we get $n \approx 1.39$, which is within the range for real devices.

In the second-quadrant, the MS junction is reverse biased and the current decreases exponentially with the voltage. The current is eventually saturated at approximately 0.4 nA.

Figure 4.14 (b) shows the semi-logarithmic plot of *I-V* curve under OM light illumination. The *I-V* curves of dark and under OM illumination differ in two main aspects. First, with the same voltage range, in the first-quadrant, the curve more straight and the region 3 is absent. Second, the short circuit current was shifted to the higher voltage value.

In summary, the *I-V* measurements exhibit the potential of the electrical properties of droplet on semiconductor surface that needs to be explored further. For example, to obtain the Schottky barrier height, the temperature dependence measurement must be conducted [91] and the measurements of the other systems—e.g., In droplet on InAs or Ga droplet on GaSb—will provide the valuable informations.

4.5 Manipulation of Self-Running Ga Droplets Migration

Apart from the electrical properties, in two experiments, to manipulate self-running Ga droplets migration, CHPs are grown underneath the GaAs sacrificed layer as described in Section 3.1.5. The sublimation results of these samples are presented in this Section.

4.5.1 Manipulation of Droplets Migration in MBE

Surface morphology of sample 9 after sublimation in MBE is shown in Figure 4.15. We clearly found the formation of CHPs as marked with dashed lines in Figure 4.15(b). The interesting results are the formation of Ga droplets and the running direction of droplets in this sample.

We found the ordering formation of Ga droplets as shown in Figure 4.15(a). Ga droplets form along strain-relaxed sites, in good agreements with the previous study of controlled Ga droplets nucleation by strain distribution [92]. Some of these Ga droplets already run, while others just form.

The Ga droplets run in two distinct directions: along [-110] for those on strain-relaxed sites and [110] or [-1-10] for those on the edge of sample. The DIC image from the edge of sample is taken from the exposed areas—occured due to the sample scribing—for confirmation of running direction without the effect of strain-relaxed sites that should follows the previous studies[4-6, 22]—along [110] or [-1-10]. Droplet 2 in Figure 4.15(c) run along [110], leaving a running trail of about 4 μm. In contrast, above strain-relaxed sites, droplet 1 in Figure 4.15(a) runs along [-110], leaving a longer trail of about 8 μm. In addition, the direction of droplet 3 in Figure 4.15(b) deviates about 25° from [-110] to [-1-10].

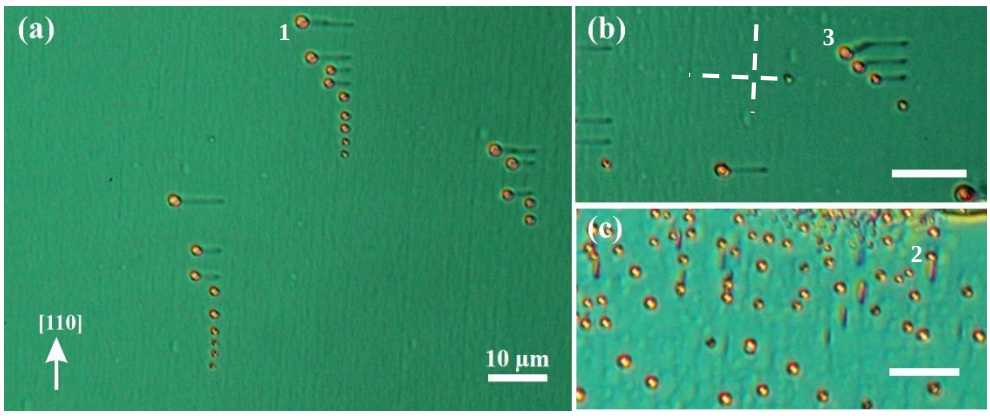

Figure 4.15 The DIC images showing self-running Ga droplets on a 100 nm GaAs(001) grown above 25 nm $In_{0.2}Ga_{0.8}As$ CHPs that (a) run along [-110], (b) one droplet run in a deviated direction, and (c) run along [110] and [-1-10] at exposed region in the edge of sample. The scale bars are 10 μm.

Surface morphology of sample 10 after sublimation in MBE is shown in Figure 4.16. The CHPs are not clearly seen in this sample, possibly because the GaAs sacrificed layer is too thick.

The Ga droplets run relatively similar to those of sample sample 9 with more clear turning evidences. Droplet 1 in Figure 4.16(a) runs along [110] about 7 μm before finally turns about 65° to [1-10]. Figure 4.16(b) shows the distinct running directions of two droplets in one frame: droplet 2 and 3 run along [-1-10] and [1-10], respectively. In addition, the direction of droplet 4 deviates about 25° from [110] to [-110] as shown in Figure 4.16(c).

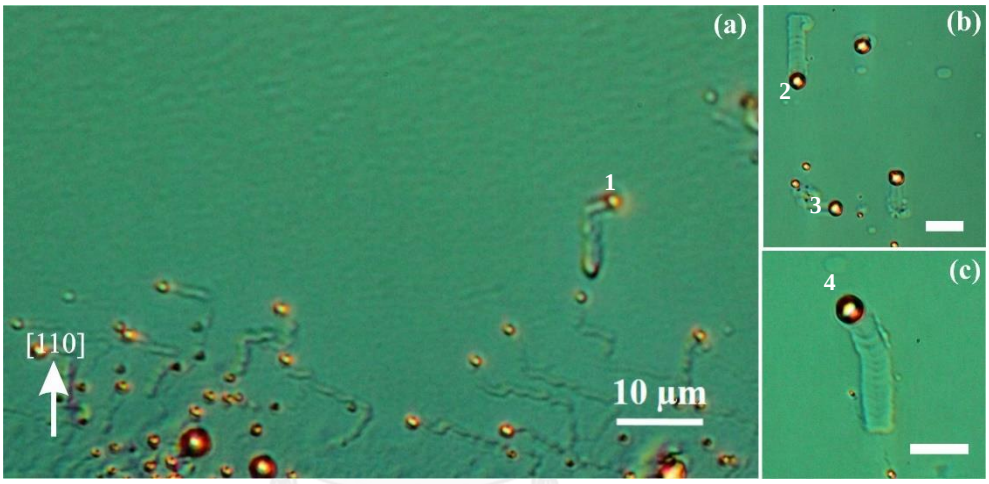

Figure 4.16 The DIC images showing self-running Ga droplets on a 300 nm GaAs(001) grown above 25 nm $In_{0.2}Ga_{0.8}As$ CHPs that (a) run and turn, (b) droplets run in two different directions, and (c) a droplet runs non-straightly. The scale bars are 10 μm.

Our observation proves the possibility of manipulation of droplet running migration, however to really prove the hypothesis, the sample must be real-time imaged in LEEM. After sublimation in MBE, surface of samples 9 and 10 still having enough space for droplet to run. Therefore, the sublimation was continued in LEEM as further shown in Section 4.5.2.

4.5.2 Manipulation of Droplets Migration in LEEM

This Sections reports the results of samples sublimation in LEEM which are divided into two Subsections. Subsection 4.5.2.1 shows the real-time oxides desorption and Subsection 4.5.2.2 presents the running Ga droplets realization.

4.5.2.1 Real-Time Thermal Oxides Desorption

We already know that thermal desorption of native oxides layer on GaAs occurs twice from Section 4.1.1 but we do not really know the real-time surface condition of sample in MBE. In LEEM, we can not clearly see the As oxides desorption due to the gas phase of As oxides, however we can clearly see the Ga oxides desorption as shown in Figure 4.17. This section only show the Ga oxides desorption of sample 9 since sample 10 undergoes the similar condition during the oxides desorption.

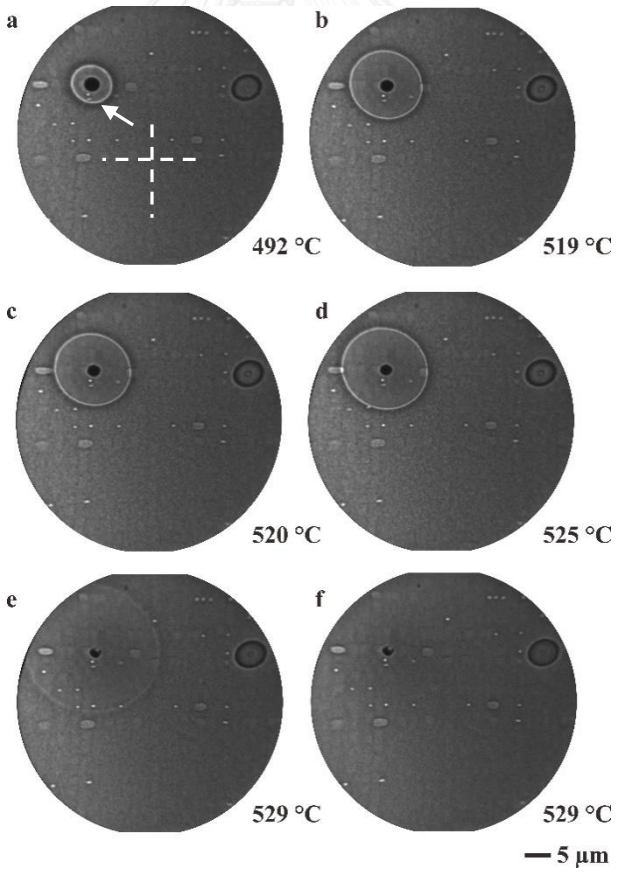

Figure 4.17 The MEM images of Ga oxides desorption of sample 9 in LEEM.

A Ga droplet—resulted from MBE sublimation—appears as a black circle surrounded by the oxide layer that appears as a bright circle, marked with arrow in Figure 4.17(a). CHPs are also vaguely visible as marked with dashed lines in Figure 4.17(a).

The oxides layer desorption starts from the Ga droplet. As the temperature increases to 525 °C, the bright circle grows bigger and the residual gas analyzer (RGA) reading of Ga increases. Ga is difficult to evaporate at ~500 ºC, excepts in the form of molecules—e.g., $3Ga_2O$ or Ga_2O_3 [75]. So the increasing of RGA reading for Ga is attributed to the desorption of native Ga oxides. Afterward, at temperature of about 529 °C, the bright circle becomes dimmer and eventually disappears as shown in Figure 4.17(e) and 4.17(f). The RGA reading of Ga also decreases, indicating the end of the Ga oxides desorption. In addition, temperature difference between the latter—the point where Ga oxides completely removed—in Figure 4.17(f) and the former—the starting point of the Ga oxides removal—in Figure 4.17(a) of oxides desorption is approximately 30 °C, proving the usage of Ga oxides desorption at 610 °C (30 °C above the theoritical oxides desorption temperature) is effective for removing the Ga oxides [93, 94].

An equivalent result has been reported for the thermal native oxides desorption on GaP surface: the oxides removal starts from a defect on the surface [95]. The shape of oxide layer during desorption depends on the shape of structure on the surface. In the former result of GaP surface, the layer appears as a long line instead of bright circle as in our sample.

4.5.2.2 Sublimation in LEEM

After thermal desorption of native oxides layer, the increasing of temperature brings the surface to a non-congruent evaporation stage at T_c of about 630 °C as shown in Figure 4.18(a). In this stage, Ga droplets start to nucleate and clusterize on the surface. They grow bigger when the temperature further increases above T_c.

After reaching a critical size that is similar to the previous study about 2 μm [5], the droplets start to run as shown in Figure 4.18(c). Next to allow the droplets run further without any new droplet formation, the temperature was held at 637 °C for several minutes as shown in Figures 4.18(d) to 4.18(f). Surprisingly, of the many

observed running droplets, there were no droplets turning as previously seen in Figure 4.15—CHPs are also somehow disappeared from the surface. The droplets just run along one majority direction, which is unknown during in situ LEEM imaging.

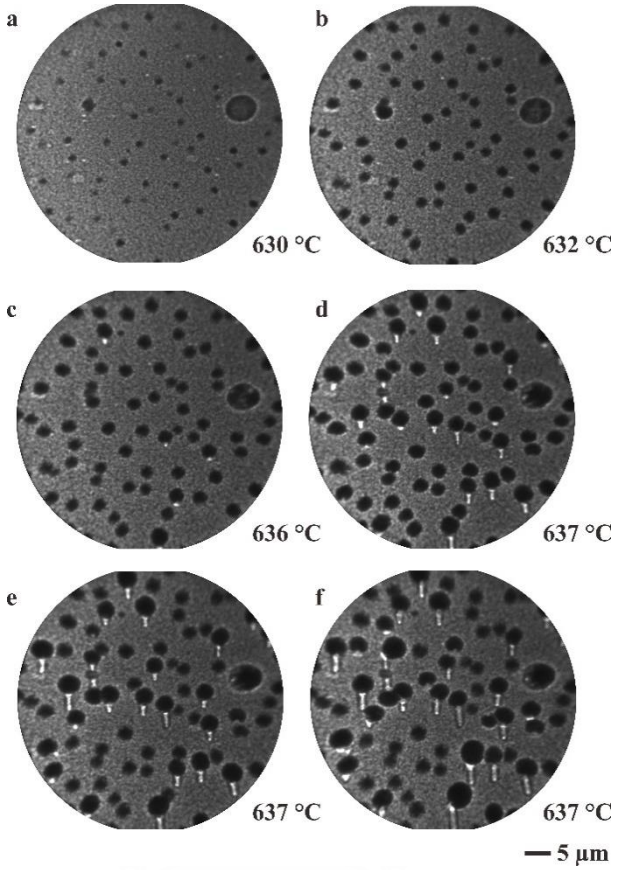

Figure 4.18 The sublimation of sample 9 in LEEM.

In contrast to sample 9, sample 10 shows the turnings of Ga droplets upon sublimation between T_c and T_c+20 °C—in this experiment, T_c is ~640 ºC. Figure 4.19 shows MEM snapshots of two droplets that make a turning during sublimation of sample 10.

Figure 4.19(a) captures the movements of droplet 1 for about 33 min. At first, the droplet move toward a majority direction which is possibly along the [110] or [-1-10]. After 2 min running, it stops running onto this direction and starts to run sideway. Finally, it makes another sideway turn and runs towards the reverse initial direction (U-turn). From the trail length, the average speed of droplet 1 is about 0.45 µm/min.

Figure 4.19(b) captures the movements of droplet 2 for about 42 min. Analogous to droplet 1, droplet 2 initially run toward a majority direction. After 36

running, it starts to make 45°-turn and finally runs further at this direction for about 6 min. From the trail length, the average speed of droplet 2 is much slower droplet 1 about 0.21 μm/min.

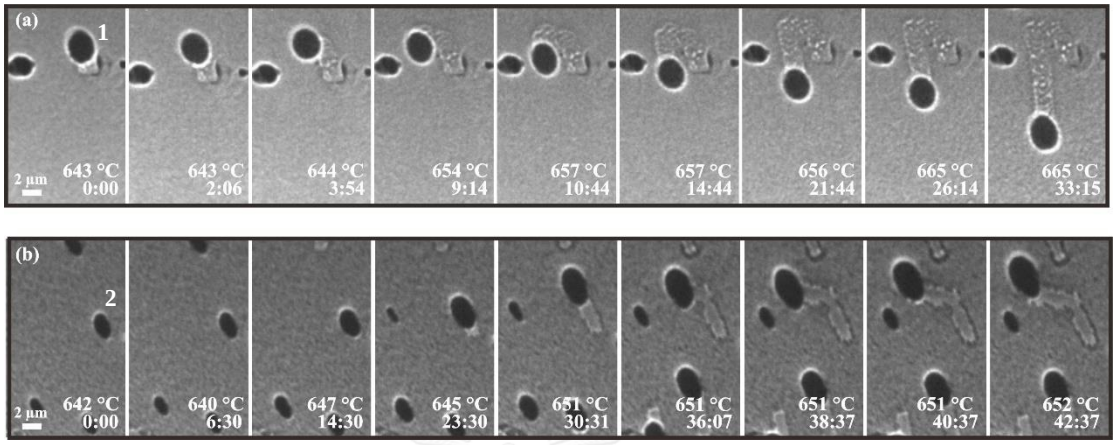

Figure 4.19 Time-lapse of MEM snapshots during sublimation of sample 10 showing Ga droplet that makes a (a) U-turn and (b) 45°-turn. The time at the bottom is in min:sec, relative to the left-most image.

To know the exact direction of droplets and to study the surface morphology of samples 9 and 10, each sample is imaged ex situ by DIC microscopy.

4.5.3 Ex-situ DIC analyses

Figure 4.20 shows the post-sublimated surface morphology of sample 9. It can be inferred that the droplets run along [110] or [-1-10] and the CHPs are somehow disappeared from the surface. In addition, there is no evidence of droplets turning as previously seen in Figure 4.15.

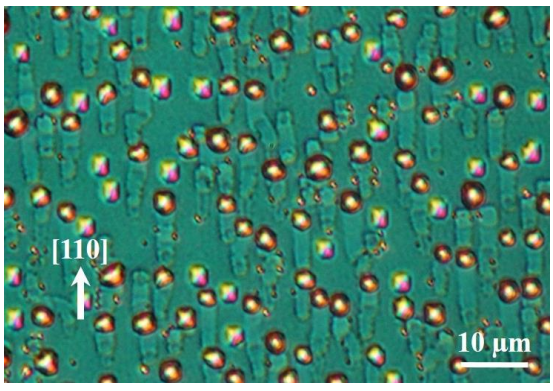

Figure 4.20 The DIC image showing surface morphology of sample 9 after sublimation in LEEM.

The absent of droplet turning is attributed to two possibilities. First, CHPs are not really formed underneath the GaAs sacrificed layer or the sublimation makes the disappeared CHPs. Second, the Ga droplets are too big and the dislocations are too deep so that the droplets easily cross over the dislocations as previously explained in Section 2.5.3.

Figure 4.21 shows the post-sublimated surface morphology of sample 10. In contrast to sample 9, the surface is populated by running Ga droplets with almost random directions. Droplet 1 in Figure 4.21 runs toward [110] while only few microns from this droplet, droplet 2 runs toward [-110]. In addition, we also observe the turning and the directionless movements of droplets as shown in droplets 3 and 4, respectively.

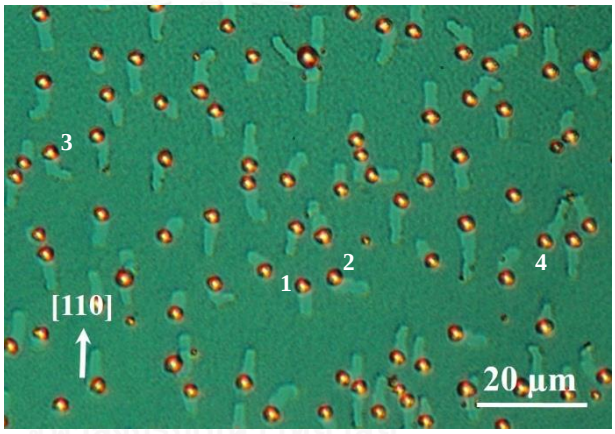

Figure 4.21 The DIC image showing surface morphology of sample 9 after sublimation in LEEM.

Figure 4.22 shows four turnings of Ga droplets in sample 10: (a) two successive sideway turns (b) a U-turn following by a sideway turn, (c) a sideway turn following by sharp V-turn, and (d) a 110°-turn. These turnings are kinematically impossible, except there is any disturbance on the GaAs surface.

The latter under DIC microcope, we reveal large Ga-rich regions underneath GaAs surface, indicating Ga spits occur during growth. There is no evidence of CHPs, however Ga spits result in the formation of defects [96-98] and may vary the surface properties as well—e.g., chemical or physical properties.

As we have shown in Section 2.5.2, when a droplet surrounded by the chemically-, thermally-, or otherwise-induced non-uniform surfaces, the two

directionality responsible forces of droplet: F_{diff} and F_{drift} will be imbalance. The droplet will run toward the maximum force F_m.

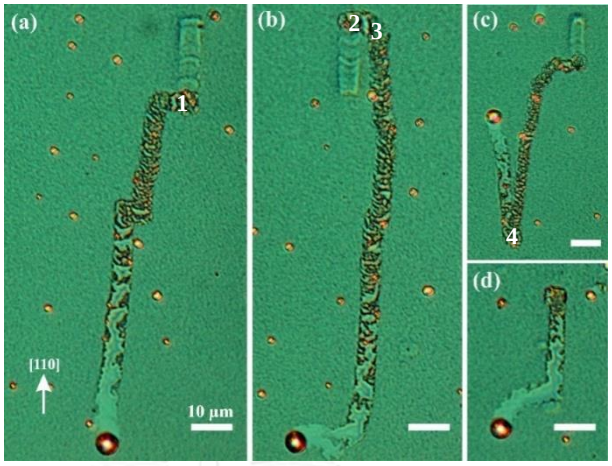

Figure 4.22 The DIC images showing turnings of Ga droplet in sample 9. The scale bars are 10 μm.

For the explanation of these turning droplets, at some areas of GaAs F_m is stronger than F_{diff}, causing the droplet runs out of the diffusion barrier direction. While at some areas F_m is weaker than F_{diff}, so that the droplet runs back along the diffusion barrier direction.

For the sideway turn: at first F_{diff} is dominant toward [-1-10] until the droplet reaches the area marked with 1 in Figure 4.22(a) and F_m becomes stronger than F_{diff}, causing the droplet run along [-110]. For the U-turn as exemplified by markers 2 and 3 in Figure 4.22(b): initially at 2, F_m toward [1-10] is stronger than F_{diff} toward [110] and finally at 3, F_{diff} toward reverse initial direction of [-1-10] is dominant. For the sharp V-turn: at first F_{diff} is dominant toward [-1-10] until the droplet reaches the area marked with 4 in Figure 4.22(c) and and F_m becomes dominant.

In summary, regardless of the absent of CHPs, we still have shown striking results about manipulation of running Ga droplets migration on GaAs (001). For the first time, we showed that Ga droplets on GaAs (001) not only runs in the [110] or [-1-10] as previously reported [4-6, 22] but also in others direction dictated by F_{diff} and F_{drift}.

CHAPTER 5
Summary and Outlook

A simple procedure to produce self-running Ga droplets on GaAs (001) in MBE has been rigorously discussed through a series of experiments. The procedure relies on the observation of RHEED patterns and registration of a reference temperature used in the subsequent sublimation conditions.

The three stages of RHEED pattern evolution may be explained as follows. The first RHEED pattern observed is a broad, streaky pattern where the underlying cause is thermal desorption of native oxides; the AFM image shows the surface corrugation at this stage. At the reference temperature T_0, the second RHEED pattern appears as a chevron pattern and the AFM image shows the nanoscale Ga droplets formation. Above T_0, the RHEED pattern decay and disappear where the underlying cause is the formation of liquid phase Ga droplets, diffusing the electron beam from the RHEED gun [80, 99].

After that, the procedure applies the sublimation temperature and time around T_0 to obtain self-running Ga droplets. The procedure successfully produces self-running Ga droplets in the tested samples with four different temperature profiles. The procedure also explains the mechanism for reducing the number of secondary droplets by keeping the temperature above T_0 momentarily and then sublimated below T_0.

The procedure may have technological advantages and open up new studies for droplet-based growth in MBE. With the procedure, self-running Ga droplets can be routinely realized and combined with other processes such as Stranki-Krastanov or droplet epitaxy, creating many new nanoelectronic structures and device architectures.

The selective Ga droplets etching, the fabrication of sharp W tip, and the *I-V* characterization have been reported. For the selective Ga droplets etching, 15 min etching in a HCl:H_2O (1:2) solution—with stirring—was found to effectively remove the Ga droplets while only negligibly amount of GaAs was etched. This recipe may be useful for further Ga droplet removal studies. For the fabrication of sharp W tip, a tip diameter as small as 1 μm can be obtained using electrochemical etching reaction. This tip not only can be used for *I-V* characterization but also for other purposes e.g.,

as a probe of surface microscopy and microscopic tweezers. For the *I-V* characterization, the electrical properties of Ga droplet on GaAs surface follow a Schottky characteristic. This result is useful as initial study of droplet electrical properties that needs to be explored further. For example, to obtain the Schottky barrier height, the temperature dependent measurement must be conducted and the measurements of the other systems—e.g., In droplet on InAs or Ga droplet on GaSb—will provide a comparison information. In addition, the emission spectrum of light from Ga droplet on GaAs surface is also important and should be measured.

A manipulation of running Ga droplets migration on GaAs (001) has been presented by combining the MBE based growth and the real time sublimation in LEEM. The manipulation of running Ga droplets can be improved by ensuring the formation of CHPs underneath GaAs sacrificial layer to obtain controlled running direction. The directions of droplets in our experiments are only partially controlled since the CHPs are not properly formed as a result of Ga spitting during the growth of the CHPs layer.

REFERENCES

1. Ekimov, A. and A. Onushchenko, *Quantum size effect in the optical-spectra of semiconductor micro-crystals.* Soviet Physics Semiconductors-USSR, 1982. **16**(7): p. 775-778.
2. Nozawa, T. and Y. Arakawa, *Detailed balance limit of the efficiency of multilevel intermediate band solar cells.* Applied Physics Letters, 2011. **98**(17): p. 171108.
3. Law, M., J. Goldberger, and P. Yang, *Semiconductor nanowires and nanotubes.* Annu. Rev. Mater. Res., 2004. **34**: p. 83-122.
4. Tersoff, J., D.E. Jesson, and W.X. Tang, *Running droplets of gallium from evaporation of gallium arsenide.* Science, 2009. **324**(5924): p. 236-8.
5. Wu, J., et al., *Critical size of self-propelled motion of droplets on GaAs (100) surface.* Journal of Applied Physics, 2012. **112**(4): p. 043523.
6. Wu, J., et al., *Nanoscale footprints of self-running gallium droplets on GaAs surface.* PLoS One, 2011. **6**(6): p. e20765.
7. Shao, Y., et al., *Behavior of Au-Si droplets in Si (001) at high temperatures.* Applied Physics Letters, 2012. **101**(5): p. 053104.
8. Lee, E., et al., *Formation of self-assembled large droplet-epitaxial GaAs islands for the application to reduced reflection.* Journal of Applied Physics, 2013. **113**(15): p. 154308.
9. Pillai, S., et al., *Surface plasmon enhanced silicon solar cells.* Journal of applied physics, 2007. **101**(9): p. 093105.
10. Wu, J., et al., *Intersublevel infrared photodetector with strain-free GaAs quantum dot pairs grown by high-temperature droplet epitaxy.* Nano letters, 2010. **10**(4): p. 1512-1516.
11. Cavigli, L., et al., *Individual GaAs quantum emitters grown on Ge substrates.* Applied physics letters, 2011. **98**(10): p. 103104.
12. Hilner, E., et al., *Ordering of the nanoscale step morphology as a mechanism for droplet self-propulsion.* Nano Lett, 2009. **9**(7): p. 2710-4.

13. Kanjanachuchai, S. and C. Euaruksakul, *Self-running Ga droplets on GaAs (111)A and (111)B surfaces.* ACS Appl Mater Interfaces, 2013. **5**(16): p. 7709-13.
14. Shorlin, K. and M. Zinke-Allmang, *Shape cycle of Ga clusters on GaAs during coalescence growth.* Surface science, 2007. **601**(12): p. 2438-2444.
15. Li, M.Y., et al., *Formation of Ga droplets on patterned GaAs (100) by molecular beam epitaxy.* Nanoscale Res Lett, 2012. **7**(1): p. 550.
16. Tersoff, J., D.E. Jesson, and W.X. Tang, *Decomposition controlled by surface morphology during langmuir evaporation of GaAs.* Phys Rev Lett, 2010. **105**(3): p. 035702.
17. Bain, C.D., G.D. Burnett-Hall, and R.R. Montgomerie, *Rapid motion of liquid drops.* Nature, 1994. **372**(6505): p. 414-415.
18. Chaudhury, M.K. and G.M. Whitesides, *How to make water run uphill.* Science, 1992. **256**(5063): p. 1539-1541.
19. Dos Santos, F.D. and T. Ondarcuhu, *Free-running droplets.* Physical review letters, 1995. **75**(16): p. 2972.
20. Li, S., et al., *Thermal etching process of microscale pits on the GaAs (001) surface.* physica status solidi (RRL)-Rapid Research Letters, 2012. **6**(1): p. 25-27.
21. Lee, J., Z.M. Wang, and G. Salamo, *Ga-triggered oxide desorption from GaAs (100) and non-(100) substrates.* Applied physics letters, 2006. **88**(25): p. 252108.
22. Wu, J., et al., *On the secondary droplets of self-running gallium droplets on GaAs surface.* ACS Appl Mater Interfaces, 2011. **3**(6): p. 1817-20.
23. Zheng, C., W.-X. Tang, and D. Jesson, *Asymmetric coalescence of reactively wetting droplets.* Applied Physics Letters, 2012. **100**(7): p. 071903.
24. Rowlinson, J.S. and B. Widom, *Molecular theory of capillarity*. 2013: Courier Dover Publications.
25. Kanjanachuchai, S. and C. Euaruksakul, *Directions and Breakup of Self-Running In Droplets on Low-Index InP Surfaces.* Crystal Growth & Design, 2014. **14**(2): p. 830-834.

26. Kanjanachuchai, S. and P. Photongkam, *Dislocation-Guided Self-Running Droplets.* Crystal Growth & Design, 2015. **1 (2015)**: p. 14–19.
27. Mandl, B., et al., *Growth Mechanism of Self-Catalyzed Group III− V Nanowires.* Nano letters, 2010. **10**(11): p. 4443-4449.
28. Abrahams, M. and C. Buiocchi, *Etching of dislocations on the low-index faces of GaAs.* Journal of Applied Physics, 1965. **36**(9): p. 2855-2863.
29. Zeng, D., et al., *Type and formation mechanism of thermal etch pit on annealed (111) CdZnTe surface.* Thin Solid Films, 2009. **517**(9): p. 2896-2899.
30. Kumar, G. and K.N. Prabhu, *Review of non-reactive and reactive wetting of liquids on surfaces.* Advances in colloid and interface science, 2007. **133**(2): p. 61-89.
31. Assael, M.J., et al., *Reference data for the density and viscosity of liquid cadmium, cobalt, gallium, indium, mercury, silicon, thallium, and zinc.* Journal of Physical and Chemical Reference Data, 2012. **41**(3): p. 033101.
32. Hong, X., X. Gao, and L. Jiang, *Application of superhydrophobic surface with high adhesive force in no lost transport of superparamagnetic microdroplet.* J Am Chem Soc, 2007. **129**(6): p. 1478-9.
33. Dong, L., A. Chaudhury, and M.K. Chaudhury, *Lateral vibration of a water drop and its motion on a vibrating surface.* Eur Phys J E Soft Matter, 2006. **21**(3): p. 231-42.
34. Pratap, V., N. Moumen, and R.S. Subramanian, *Thermocapillary motion of a liquid drop on a horizontal solid surface.* Langmuir, 2008. **24**(9): p. 5185-5193.
35. Brzoska, J., F. Brochard-Wyart, and F. Rondelez, *Motions of droplets on hydrophobic model surfaces induced by thermal gradients.* Langmuir, 1993. **9**(8): p. 2220-2224.
36. Andrews, A., et al., *Modeling crosshatch surface morphology in growing mismatched layers. Part II: Periodic boundary conditions and dislocation groups.* Journal of applied physics, 2004. **95**(11): p. 6032-6047.
37. Adachi, S., *Properties of semiconductor alloys: group-IV, III-V and II-VI semiconductors*. Vol. 28. 2009: John Wiley & Sons.

38. Nakareseisoon, N., et al. *Self-assembled nanoholes on cross-hatch patterns templates for quantum dot solar cells*. in *The 37th Electrical Engineering Conference (EECON-37)*. 2014. Khon Kaen University.
39. Jittrong, A., et al. *Self-Assembled InAs Quantum Dots Approaching Rectangular Shapes with Multi-Stacked Growth*. in *The 37th Electrical Engineering Conference (EECON-37)*. 2014. Khon Kaen University.
40. Limwongse, T., et al., *InGaAs quantum dots on cross-hatch patterns as a host for diluted magnetic semiconductor medium.* Journal of Nanomaterials, 2013. **2013**: p. 3.
41. Andrews, A., et al., *Modeling cross-hatch surface morphology in growing mismatched layers.* Journal of applied physics, 2002. **91**(4): p. 1933-1943.
42. Wilkinson, A.J., *Observation of strain distributions in partially relaxed In0. 2Ga0. 8As on GaAs using electron channelling contrast imaging.* Philosophical magazine letters, 1996. **73**(6): p. 337-344.
43. Hull, D. and D.J. Bacon, *Introduction to dislocations*. Vol. 257. 1984: Pergamon Press Oxford.
44. Thet, C.C., et al., *Development of Cross-hatch Pattern on InGaAs/GaAs Virtual Substrate.*
45. Ayers, J.E., *Heteroepitaxy of semiconductors: theory, growth, and characterization*. 2007: CRC press.
46. Barabasi, A.-L., *Thermodynamic and kinetic mechanisms in self-assembled quantum dot formation.* Materials Science and Engineering: B, 1999. **67**(1): p. 23-30.
47. Uchida, Y., H. Kakibayashi, and S. Goto, *Electrical and structural properties of dislocations confined in a InGaAs/GaAs heterostructure.* Journal of applied physics, 1993. **74**(11): p. 6720-6725.
48. Neamen, D.A. and B. Pevzner, *Semiconductor physics and devices: basic principles*. Vol. 3. 2003: McGraw-Hill New York.
49. Tung, R.T., *The physics and chemistry of the Schottky barrier height.* Applied Physics Reviews, 2014. **1**(1): p. 011304.

50. Bayhan, H. and A.S. Kavasoglu, *Exact analytical solution of the diode ideality factor of a pn junction device using Lambert W-function model.* Turkish Journal of Physics, 2007. **31**(1): p. 7-10.

51. Dakin, J.P. and R.G. Brown, *Handbook of Optoelectronics (two-volume set).* 2006: CRC Press.

52. Raynaud, C., et al., *Barrier height determination of SiC Schottky diodes by capacitance and current–voltage measurements.* Journal of applied physics, 2002. **91**(12): p. 9841-9847.

53. Jesson, D. and W.-X. Tang, *Surface electron microscopy of Ga droplet dynamics on GaAs (001).* Microscopy: Science, Technology, Applications and Education, 2010: p. 1608-1619.

54. Barron, A.R. *Chemistry of Electronic Materials*. Molecular Beam Epitaxy 2011 10/08/2011 [cited 2015 23/02/2015]; Available from: http://cnx.org/contents/1096167b-8518-4159-a88d-3b2ae4df6645@9.1:28/Chemistry_of_Electronic_Materi.

55. Nabetani, Y., et al., *Initial growth stage and optical properties of a three-dimensional InAs structure on GaAs.* Journal of applied physics, 1994. **76**(1): p. 347-351.

56. SLRI. *BL3.2b : Photoemission Electron Microscopy (PEEM)*. [cited 2015 23/02/2015]; Available from: http://www.slri.or.th/en/index.php?option=com_content&view=article&id=41&Itemid=96.

57. Technology, O.I.o.S.a. *LEEM / PEEM*. 2014 [cited 2015 23/02/2015]; Available from: https://groups.oist.jp/fsu/leem-peem.

58. de la Figuera, J. and K.F. McCarty, *Low-Energy Electron Microscopy*, in *Surface Science Techniques*. 2013, Springer. p. 531-561.

59. Prostrednik, D. and P. Osanna, *Nanometrology for industrial applications.* e&i Elektrotechnik und Informationstechnik, 1998. **115**(4): p. 213-217.

60. Liljeborg, A. *Optics for Differential Interference Contrast (DIC)*. 2012 [cited 2015 24/02/2015]; Available from: http://www.nanophys.kth.se/nanophys/facilities/nfl/nikon-me600/incident/dicincid.html.

61. Binnig, G., C.F. Quate, and C. Gerber, *Atomic force microscope.* Phys Rev Lett, 1986. **56**(9): p. 930-933.
62. Martin, Y., C. Williams, and H.K. Wickramasinghe, *Atomic force microscope–force mapping and profiling on a sub 100-Å scale.* Journal of Applied Physics, 1987. **61**(10): p. 4723-4729.
63. Deng, Z. *Basic Principle of Scanning Probe Microscopy*. 2011 [cited 2014; Available from: http://www.qilerongrong.org/Pro_Zhao.html.
64. Schneider, C.A., W.S. Rasband, and K.W. Eliceiri, *NIH Image to ImageJ: 25 years of image analysis.* Nature methods, 2012. **9**(7): p. 671-675.
65. Horcas, I., et al., *WSXM: a software for scanning probe microscopy and a tool for nanotechnology.* Review of Scientific Instruments, 2007. **78**(1): p. 013705.
66. Kalantar-zadeh, K. and B. Fry, *Nanotechnology-enabled sensors*. 2007: Springer Science & Business Media.
67. Facility, A.M.M.R. *SEM layout and function*. 2013 15/03/2013 [cited 2015 24/02/2015]; Available from: http://www.ammrf.org.au/myscope/sem/practice/principles/layout.php#detail.
68. Goldstein, J.I., et al., *Scanning electron microscopy and X-ray microanalysis. A text for biologists, materials scientists, and geologists*. 1981: Plenum Publishing Corporation.
69. Elborg, M., et al., *Self-assembly of Ga droplets attached to GaAs quantum dots.* Journal of Crystal Growth, 2013. **378**: p. 53-56.
70. Shockley, W., *Electrons and holes in semiconductors.* 1953.
71. Zoski, C.G., *Handbook of electrochemistry*. 2007: Elsevier.
72. Atkins, P.W. and P.W. Atkins, *The elements of physical chemistry*. 1992: Oxford University Press Oxford United Kingdom.
73. Haynes, W.M., *CRC handbook of chemistry and physics*. 2011: CRC Press.
74. Ibe, J., et al., *On the electrochemical etching of tips for scanning tunneling microscopy.* Journal of Vacuum Science & Technology A, 1990. **8**(4): p. 3570-3575.
75. Guillén-Cervantes, A., et al., *GaAs surface oxide desorption by annealing in ultra high vacuum.* Thin Solid Films, 2000. **373**(1): p. 159-163.

76. Yamada, M. and Y. Ide, *Anomalous behaviors observed in the isothermal desorption of GaAs surface oxides.* Surface science, 1995. **339**(3): p. L914-L918.

77. Blumin, M., et al., *Self-assembled InAs quantum dots and wires grown on a cleaved-edge GaAs (110) surface.* Journal of applied physics, 2006. **99**(9): p. 093518.

78. Yao, H., P.G. Snyder, and J.A. Woollam, *Temperature dependence of optical properties of GaAs.* Journal of applied physics, 1991. **70**(6): p. 3261-3267.

79. Ruterana, P., M. Albrecht, and J. Neugebauer, *Nitride semiconductors.* Handbook on Materials and Devices, 2003.

80. Nemcsics, Á., *In-Situ Investigation of the Growth of Low-Dimensional Structures*, in *Towards Intelligent Engineering and Information Technology*. 2009, Springer. p. 557-572.

81. Trisna, B.A., et al. *The Effect of Temperature Non-uniformities on Self-Running Gallium Droplets*. in *The 37th Electrical Engineering Conference (EECON-37)*. 2014. Khon Kaen University.

82. Zinke-Allmang, M., L. Feldman, and W. Van Saarloos, *Experimental study of self-similarity in the coalescence growth regime.* Physical review letters, 1992. **68**(15): p. 2358.

83. Riesz, F., L. Dobos, and J. Karanyi, *Thermal decomposition of bulk and heteroepitaxial (100) InP surfaces: A combined in situ scanning electron microscopy and mass spectrometric study.* Journal of Vacuum Science & Technology B, 1998. **16**(5): p. 2672-2674.

84. Yuan, Y. and T.R. Lee, *Contact angle and wetting properties*, in *Surface science techniques*. 2013, Springer. p. 3-34.

85. Seemann, R., et al., *Wetting morphologies at microstructured surfaces.* Proceedings of the National Academy of Sciences of the United States of America, 2005. **102**(6): p. 1848-1852.

86. Ratke, L. and P.W. Voorhees, *Growth and coarsening: Ostwald ripening in material processing*. 2002: Springer Science & Business Media.

87. Quaade, U. and L. Oddershede, *Electrochemical etching of sharp tips for STM reveals singularity.* EPL (Europhysics Letters), 2002. **57**(4): p. 611.

88. Zhang, R. and D. Ivey, *Preparation of sharp polycrystalline tungsten tips for scanning tunneling microscopy imaging.* Journal of Vacuum Science & Technology B, 1996. **14**(1): p. 1-10.

89. Bashar, S.A., *Study of indium tin oxide (ITO) for novel optoelectronic devices.* UMIST, Manchester, 1998: p. 106-109.

90. Pederson, D.O. and K. Mayaram, *Analog integrated circuits for communication: principles, simulation and design*. 2007: Springer Science & Business Media.

91. Naik, S.S. and V.R. Reddy, *Temperature dependency and current transport mechanisms of Pd/V/n-type InP schottky rectifiers.* Advanced Materials Letters, 2012. **3**(3): p. 188-196.

92. Oyama, N., et al., *Proposal of selective growth technique using periodic strain field caused by misfit dislocations.* Japanese journal of applied physics, 2004. **43**(11A): p. L1422.

93. Jevasuwan, W., S. Ratanathammapan, and S. Panyakeow, *InP Ring-Shaped Quantum Dot Molecules by Droplet Epitaxy*, in *Quantum Dot Molecules*. 2014, Springer. p. 29-49.

94. Lee, J., Z.M. Wang, and G. Salamo, *Survival of atomic monolayer steps during oxide desorption on GaAs (100).* Journal of applied physics, 2006. **100**(11): p. 114330.

95. Stierle, A., H.-D. Carstanjen, and S. Hofmann, *Structural and chemical characterization on the nanoscale*, in *Nanoelectronics and Information Technology. Advanced Electronic Materials and Novel Devices*. 2012, Wiley-VCH. p. 233-254.

96. Lytvyn, P., et al., *Microsize defects in InGaAs/GaAs (N11) A/B multilayers quantum dot stacks.* Journal of crystal growth, 2005. **284**(1): p. 47-56.

97. Shinohara, M. and T. Ito, *Thermodynamic study on the origin of oval defects in GaAs grown by molecular-beam epitaxy.* Journal of Applied Physics, 1989. **65**(11): p. 4260-4267.

98. Wood, C., et al., *On the origin and elimination of macroscopic defects in MBE films.* Journal of Crystal Growth, 1981. **51**(2): p. 299-303.

99. Rudas, I.J., J. Fodor, and J. Kacprzyk, *Towards intelligent engineering and information technology*. Vol. 243. 2009: Springer Science & Business Media.

100. Ekvall, I., et al., *Preparation and characterization of electrochemically etched W tips for STM.* Measurement Science and Technology, 1999. **10**(1): p. 11.

APPENDIX

The Chemical Preparations

The following is a procedure of the chemical solution preparations required throughout the electrochemical W tip and the selective Ga droplets etchings. Calculation of molar solution and directions of mixing are given so that the user can prepare the solution from a different starting grade of commercial chemicals.

1. The electrochemical W tip etching

Preparation of a 2 M Potassium Hydroxide (KOH) adopted from Ekvall et al. [100]

Molar mass: 56 gram/ mol

The SDRL lab uses 46% KOH (assumption: 46 gram is KOH and 54 gram is H_2O)

Density of 46% KOH is approximately 2.04 gram/ mL

Equation to get concentration (M) of KOH is

$$\left[\frac{\%\ KOH}{molar\ mass}\right] density \tag{A.1}$$

Thus,

$$\left[\frac{46\ \cancel{gram}\ KOH}{1}\right]\left[\frac{1}{100\ \cancel{gram}}\right]\left[\frac{1\ mol}{56\ \cancel{gram}}\right]\left[\frac{2.04\ \cancel{gram}}{1\ mL}\right] = 0.0167 \text{ mol/ mL} = 16.7 \text{ M} \tag{A.2}$$

Calculation of the water needed to dilute the solution

The dilution formula is

$$M_i V_i = M_f V_f \tag{A.3}$$

Where M_i is the initial concentration (M), V_i is the initial volume of solution (L), M_f is the final concentration (M), and V_f is the final volume of solution (L). Therefore, in this case, M_i is 16.7 M and M_f is 2 M. If V_i is 0.1 L, then V_f is 0.8 L. Thus, the water needed to dilute the solution is (0.8-0.1) L = 0.7 L.

Direction

Dissolve 100 mL of 46% KOH with 700 mL of deionized water (H_2O).

2. The selective Ga droplets etching

Preparation of a HCl:H_2O (1:5) solution, recipe adopted from Elborg, et al. [69]

Add 10 mL of 37% HCl to 50 mL of deionized water (H_2O).

Preparation of a HCl:H_2O (1:2) solution

Add 10 mL of 37% HCl to 20 mL of deionized water (H_2O).

List of Publications

1. International Journal

   Trisna, B. A., Nakareseisoon, N., Eiwwongcharoen, W., Panyakeow, S., & Kanjanachuchai, S. (2015). Reliable synthesis of self-running Ga droplets on GaAs (001) in MBE using RHEED patterns. Nanoscale Res Lett, 10(1), 184.

2. National Conference Papers

- Jittrong, A., Eiwwongcharoen, W., Nakareseisoon, N., **Trisna, B. A.**, Panyakeow, S., & Kanjanachuchai, S. (2014, 19-21 November 2014). *Self-Assembled InAs Quantum Dots Approaching Rectangular Shapes with Multi-Stacked Growth.* Paper presented at the The 37th Electrical Engineering Conference (EECON-37), Khon Kaen University.

- Nakareseisoon, N., **Trisna, B. A.**, Thainoi, S., Panyakeow, S., & Kanjanachuchai, S. (2014, 19-21 November 2014). Self-assembled nanoholes on cross-hatch patterns templates for quantum dot solar cells. Paper presented at the The 37th Electrical Engineering Conference (EECON-37), Khon Kaen University.

- **Trisna, B. A.**, Nakareseisoon, N., Thainoi, S., Panyakeow, S., & kanjanachuchai, S. (2014, 19-21 November 2014). The Effect of Temperature Non-uniformities on Self-Running Gallium Droplets. Paper presented at the The 37th Electrical Engineering Conference (EECON-37), Khon Kaen University.

VITA

Beni Adi Trisna was born in Karanganyar, Indonesia, on September 30, 1988. He received the Bachelor of Engineering degree in Physics Engineering from Gadjah Mada University, Indonesia, in June 2009.

Since 2009, he has been a Junior Researcher at Research Centre of Metrology, Indonesian Institute of Sciences, where he is involved in the research for development of national temperature standards. In 2013, he entered the Graduate School of Chulalongkorn University, Thailand as a Master student. Since May 2013, he has received the Chulalongkorn University (CU) Asean scholarship. His work is financial supported by Thailand's National Research University Project, Office of the Higher Education Commission (WCU-036-EN-57). His current research interests include the fabrication and characterization of semiconductor nanostructures.